buildings

MDPI

Article

Numerical Investigation of the Structural Behavior of Reinforced Concrete Deep Beams Strengthened with Fiber Reinforced Polymer (FRP) Reinforcing Bars Using the Finite Element Method

Muhammed Öztemel [1,*] and Yusuf Sümer [2]

[1] Department of Construction, Keşap Vocational School, Giresun University, 28200 Giresun, Türkiye
[2] Department of Civil Engineering, Sakarya University of Applied Sciences, 54050 Sakarya, Türkiye; ysumer@subu.edu.tr
* Correspondence: muhammed.oztemel@giresun.edu.tr

Abstract

Fiber-reinforced polymer (FRP) reinforcement has emerged as an important alternative to conventional steel due to its high corrosion resistance and long-term durability. However, studies on the behavior of FRP-reinforced concrete deep beams under shear-dominated conditions remain limited. In this study, the structural behavior of reinforced concrete deep beams strengthened with GFRP and CFRP bars was numerically investigated using the ABAQUS finite element software. A parametric analysis was conducted to evaluate the effects of shear span-to-depth ratio (a/d), concrete compressive strength, tensile reinforcement ratio, and reinforcement type. The results indicate that reducing the a/d ratio from 1.4 to 1.12 increased the maximum load capacity by 37.6% for GFRP beams and 10.0% for CFRP beams, reflecting enhanced arch action. Increasing concrete strength from 25 MPa to 40 MPa led to capacity increases of 64.5% (GFRP) and 41.7% (CFRP), confirming its dominant role. Increasing the reinforcement ratio improved capacity by 6–9% in GFRP systems and over 15% in CFRP systems. CFRP-reinforced beams exhibited 20–55% higher load capacity, while GFRP beams showed greater ultimate displacement (13–18 mm vs. 8–12 mm). Overall, CFRP provides superior strength, whereas GFRP offers enhanced ductility, supporting performance-based design.

Keywords: deep beam; FRP bars; finite element; ABAQUS; shear span-depth ratio (a/d)

Check for updates

Academic Editor: Salvatore Verre

Received: 18 March 2026
Revised: 9 April 2026
Accepted: 10 April 2026
Published: 13 April 2026

Copyright: © 2026 by the authors. Licensee MDPI, Basel, Switzerland. This article is an open access article distributed under the terms and conditions of the Creative Commons Attribution (CC BY) license.

1. Introduction

Reinforced concrete beams with a shear span-to-effective depth ratio (a/d) of 2 or less are classified as deep beams and exhibit a distinct structural behavior governed primarily by arch action rather than classical flexural theory [1]. In structural engineering practice, deep beams are widely used in critical structural applications such as high-rise buildings, transfer girders, bridge systems, and other specialized load-bearing elements. Owing to their unique load transfer mechanisms and complex stress distribution, a comprehensive understanding of their structural behavior is of considerable scientific and practical importance. Accordingly, numerous studies have been conducted to investigate the behavior of reinforced concrete deep beams under various loading and material conditions [2,3]. The load-carrying capacity of reinforced concrete deep beams is significantly influenced by key parameters, including concrete compressive strength and reinforcement ratio. However, in

aggressive environmental conditions, these structural elements are particularly susceptible to durability-related deterioration, primarily due to the corrosion of conventional steel reinforcement. The increasing use of FRP composites in reinforced concrete structures, owing to their advantageous properties such as low specific weight, high strength, and superior resistance to freeze–thaw effects, is illustrated in Figure 1 [4]. One of the primary reasons for this trend is that, under severe environmental and chemical conditions, the inadequate protection provided by the concrete cover leads to reinforcement corrosion, which in turn causes premature structural deterioration before the intended service life is achieved [4]. In this context, the corrosion process may initiate internal cracking within concrete, leading to a progressive reduction in the durability performance of the structure over time [5–8]. To mitigate this issue, fiber-reinforced polymer (FRP) reinforcements, which exhibit high resistance to corrosion, have emerged as a promising alternative, particularly in structures exposed to saline water or chemically aggressive environments [6,7]. In particular, corrosion of steel reinforcement in infrastructure systems subjected to harsh environmental exposure is one of the major causes of concrete deterioration, resulting in significant maintenance and repair costs. To address these challenges, alternative reinforcement materials such as stainless steel, epoxy-coated steel, and galvanized steel have been introduced. Nevertheless, in recent years, fiber-reinforced polymer (FRP) reinforcements have gained increasing attention as a promising alternative to conventional steel reinforcement due to their high strength-to-weight ratio and superior resistance to corrosion and freeze–thaw effects [6–8]. The use of numerical analyses supported by experimental findings enables a more efficient and cost-effective evaluation of the behavior of such structural elements. Within this framework, the primary objective of this study is to comprehensively investigate the structural performance of reinforced concrete deep beams strengthened with fiber-reinforced polymer (FRP) reinforcements. Accordingly, the main objectives of this study are defined as follows: (1) to examine the effects of concrete compressive strength, tensile reinforcement ratio, shear span-to-depth ratio (a/d), and beam geometry on structural behavior; (2) to develop a reliable finite element (FE) model capable of accurately representing the behavior of FRP-reinforced concrete deep beams; and (3) to evaluate the applicability of existing design approaches, originally developed for conventional steel-reinforced systems, to FRP-reinforced configurations. The findings of this study are expected to contribute to a better understanding of the mechanical behavior of FRP-reinforced concrete deep beams and to provide novel and scientifically valuable insights into this relatively underexplored area in the literature.

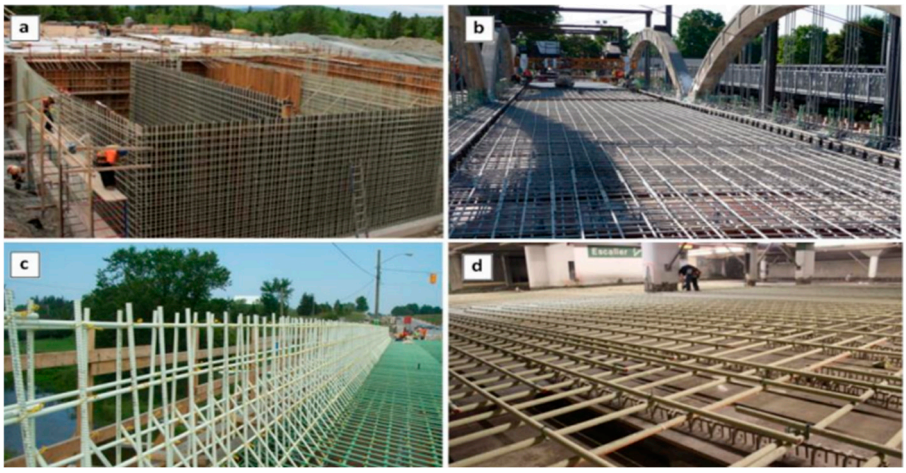


Figure 1. (**a**–**d**) Use of FRP reinforcement as an alternative reinforcement material to steel reinforcement [4].

1.1. Literature Review

Previous studies have demonstrated that the structural behavior of FRP-reinforced concrete deep beams is strongly influenced by both material properties and geometric parameters. In the study conducted by Abed et al. [9], it was reported that increasing the concrete compressive strength in reinforced concrete deep beams strengthened with longitudinal GFRP reinforcement and having compressive strengths between 43–51 MPa increased the shear capacity by approximately 44%. However, increasing the concrete compressive strength from 51 MPa to 65 MPa (a 27% increase) did not lead to a proportional increase in shear capacity, resulting in only an additional 7% increase in shear strength [8]. These findings indicate that the contribution of concrete compressive strength to shear capacity is nonlinear, particularly at higher strength levels. In another study, Abbas et al. [10] investigated the nonlinear behavior of FRP-reinforced concrete deep beams using the finite element method. In this research, eight deep beams previously tested experimentally were modeled three-dimensionally in ANSYS12.0 software, and the effects of reinforcement ratio, FRP reinforcement type, and shear span-to-depth ratio on beam behavior were evaluated. The numerical results showed good agreement with the experimental data, indicating that the developed finite element model could reliably predict the behavior of FRP-reinforced deep beams.

Similarly, Sheikh-Sobeh et al. [11] examined the behavior of GFRP-reinforced concrete deep beams using a numerical analysis approach. In this study, a three-dimensional finite element model was developed and validated using experimental results available in the literature. The effects of parameters such as concrete compressive strength, shear span ratio (a/h), and stirrup spacing on the shear strength were investigated. The results indicated that increasing concrete compressive strength and reducing stirrup spacing enhanced the shear capacity, whereas increasing the shear span ratio significantly reduced the shear strength of deep beams [11]. These results highlight the critical role of both material strength and geometric configuration in governing the shear behavior of deep beams.

Hanoon et al. [12] developed an analytical model based on the Strut-and-Tie Model (STM) to investigate the shear behavior of reinforced concrete deep beams under dynamic loading conditions. In this study, a new strut effectiveness factor based on the Mohr–Coulomb failure criterion was proposed to more accurately predict the strength of concrete compression diagonals. The developed model showed good agreement with experimental results reported in the literature and was able to reliably predict the ultimate shear strength of deep beams under different loading rates.

Kazemi et al. [13] numerically investigated the nonlinear behavior of reinforced concrete deep beams using the finite element method implemented in ABAQUS. The developed numerical models were validated through comparison with load–displacement responses obtained from experimental studies reported in the literature. Within the scope of the parametric analysis, the effects of beam height, shear span-to-depth ratio (a/h), concrete compressive strength, the presence of web reinforcement, and different types of longitudinal reinforcement (steel, GFRP, and CFRP) on stress distribution and structural performance were examined. The results indicated that an increase in the a/h ratio leads to a reduction in the load-carrying capacity of deep beams, whereas the inclusion of web reinforcement improves stress distribution and enhances the load transfer mechanism. Furthermore, CFRP reinforcement was found to provide higher stiffness and load-carrying capacity compared to GFRP reinforcement.

Similarly, the behavior of reinforced concrete deep beams reinforced with aluminium alloy (AA) bars has also been investigated in the literature using the finite element method [14]. In these studies, the developed numerical models were validated against experimental load–displacement responses, demonstrating a high level of accuracy in

predicting load-carrying capacity. The parametric investigations considered key variables including concrete compressive strength, tensile reinforcement ratio, beam geometry, a/d ratio, and transverse reinforcement ratio. The findings revealed that increasing concrete compressive strength significantly enhances shear capacity, while an increase in effective depth results in a reduction in shear strength. In addition, a strong correlation between reinforcement ratio and failure mode was observed, and the contribution of transverse reinforcement to shear capacity was clearly demonstrated. Moreover, existing design models were shown to be in good agreement with experimental results, providing reliable predictions with relatively low error margins.

In general, studies aimed at improving the shear capacity of deep beams can be broadly categorized into two main approaches. The first approach focuses on enhancing the material properties of concrete, within which the use of ultra-high-performance concrete (UHPC) has gained considerable attention. Due to its high compressive strength and fiber reinforcement, UHPC has been reported to significantly improve the shear behavior and load-carrying capacity of deep beams by enhancing the capacity of diagonal compression struts [15].

The second approach is based on the external strengthening of existing reinforced concrete elements. In this context, fiber-reinforced polymer (FRP) composites are widely utilized. In particular, materials such as GFRP and CFRP, owing to their high strength and superior corrosion resistance, have been shown to provide substantial improvements in shear capacity, stiffness, and energy absorption performance of deep beams [16].

1.2. Study Objective

FRP materials are increasingly being used in reinforced concrete systems due to their high mechanical performance and durability advantages [4]. In this context, the use of advanced numerical modeling techniques, particularly the finite element method, is of great importance for achieving a more accurate and reliable understanding of the structural behavior of FRP-reinforced deep beams. Finite element analysis can effectively capture the nonlinear response of reinforced concrete members while accounting for the linear elastic and brittle nature of FRP reinforcement, enabling a detailed evaluation of crack development, stress distribution, and failure mechanisms [17,18]. A critical review of the existing literature indicates that studies on reinforced concrete deep beams have predominantly focused on the experimental investigation of the flexural behavior of systems reinforced with GFRP bars. However, comprehensive studies addressing the combined effects of concrete compressive strength, reinforcement type (GFRP and CFRP), and geometric parameters on stress distribution remain limited. Furthermore, the influence of beam height on the flexural performance of FRP-reinforced deep beams has not been sufficiently investigated. In addition, the role of the shear span-to-depth ratio (a/h) in governing stress distribution and overall structural behavior requires further clarification. Unlike previous studies, the present study investigates not only individual parameters but also the combined and systematic effects of multiple critical variables, including concrete compressive strength, shear span-to-depth ratio (a/d), tensile reinforcement ratio, and reinforcement type (GFRP–CFRP). In this regard, the study aims to address the existing gap in the literature related to comprehensive multi-parameter and comparative analyses.

Accordingly, the primary objective of this study is to systematically investigate the nonlinear behavior of reinforced concrete deep beams strengthened with GFRP and CFRP reinforcement using advanced numerical modeling techniques. Within this framework, deep beams with different a/d ratios are analyzed, and the effects of key parameters—namely concrete compressive strength, tensile reinforcement ratio, and reinforcement type (GFRP–CFRP)—on structural performance are comprehensively evaluated.

The main contributions of this study are: (i) a multi-parameter investigation considering the combined effects of concrete strength, reinforcement type (GFRP and CFRP), and geometry; (ii) a comparative evaluation of GFRP- and CFRP-reinforced deep beams; and (iii) an assessment of load–displacement behavior, stiffness, and ultimate capacity. The findings provide insights for the design and analysis of FRP-reinforced deep beams.

2. Materials and Methods

In order to analyze the behavior of reinforced concrete deep beams in a numerical environment, the finite element method was adopted, and the analyses were carried out using the ABAQUS 2022 software. In the nonlinear three-dimensional analyses, the Concrete Damaged Plasticity (CDP) model was employed to represent the stress–strain characteristics of concrete. The extensive material and element model library provided by ABAQUS enabled realistic modeling of structural behaviors such as cracking, damage progression, and ultimate load-carrying capacity. Accordingly, the effects of FRP reinforcements on structural performance were comprehensively evaluated.

Concrete Model

Accurate modeling of the nonlinear and multiaxial mechanical behavior of concrete is of critical importance for ensuring the reliability and applicability of numerical analyses in engineering practice. In this regard, the nonlinear response of concrete under compression can be represented through constitutive approaches based on damage, plasticity, or a combination of both [19]. Plasticity refers to the irreversible deformations that remain after unloading, whereas damage is typically characterized by the degradation of elastic stiffness. The combined consideration of these two mechanisms enables a more realistic representation of the behavior of quasi-brittle materials such as concrete.

Within this framework, the Concrete Damage Plasticity (CDP) model has been widely recognized as one of the most effective and robust constitutive models for simulating the complex mechanical behavior of concrete. The CDP model integrates the concept of isotropic damage with isotropic tensile and compressive plasticity, thereby providing a unified formulation for nonlinear concrete behavior [20,21]. Two primary damage mechanisms are considered in this model: tensile cracking and compressive crushing of concrete. This dual mechanism allows for the accurate representation of both brittle fracture under tension and nonlinear deformation behavior under compression. The CDP model treats tensile and compressive responses independently and represents damage evolution through scalar damage variables, enabling the simulation of progressive stiffness degradation and material deterioration. This approach facilitates the representation of crack initiation and propagation observed in experimental studies without the need for explicit discrete crack modeling, relying instead on a continuum damage mechanics framework. Consequently, the CDP model provides a reliable and computationally efficient tool for capturing the multiaxial behavior of concrete.

In the present study, the CDP model implemented in the ABAQUS finite element software was employed to simulate the complex nonlinear behavior of concrete [22,23]. Through this approach, key damage mechanisms, including tensile cracking and compressive crushing, were effectively captured, allowing for a realistic prediction of the structural response. The model accounts for two primary damage mechanisms: cracking under tension and crushing under compression. To implement the CDP model, in addition to elastic parameters such as the elastic modulus and Poisson's ratio, five damage-related parameters must be defined. The numerical values assigned to these parameters are provided in Table 1 [22,23]. Furthermore, the density of concrete was assumed to be 2400 kg/m^3, and the Poisson's ratio was taken as 0.2 in all analyses.

Table 1. Parameters of the CDP model used in ABAQUS.

Parameter	Value
Ψ	31
ϵ	0.1
fb_0/fc_0	1.16
K	0.667
μ	0.0001

In order to accurately simulate the plastic behavior of concrete, five material parameters defined within the Concrete Damage Plasticity (CDP) model must be specified in advance. These parameters are essential for shaping the yield or failure surface of concrete [22–25]. Firstly, Ψ (dilation angle) represents the volumetric expansion that occurs during plastic flow and is defined as 31° in the scope of this study. Secondly, ε (flow potential eccentricity) is a parameter that characterizes the hyperbolic curvature of the flow surface, and it is assigned a value of 0.1. The third parameter, the fb_0/fc_0, ratio, denotes the ratio of the initial biaxial compressive strength to the initial uniaxial compressive strength of concrete, and it is modeled with a value of 1.16, consistent with the literature. The fourth parameter to be defined in the CDP model, K, represents the ratio of the second stress invariants on the tensile and compressive stress surfaces, and it is taken as 0.667 in this study. The fifth and final parameter, ν (viscosity coefficient), accounts for the time-dependent viscoplastic effects within the model and is assigned a value of 0.0001 in the present analysis. The Concrete Damage Plasticity (CDP) model, employed to represent the material behavior of concrete, is based on two primary damage mechanisms: cracking under tension and crushing under compression. These damage phenomena are defined in the model through scalar damage variables, enabling a comprehensive numerical analysis of concrete behavior under both tensile and compressive stress states. The stress–strain response associated with the CDP model is illustrated in Figure 2.

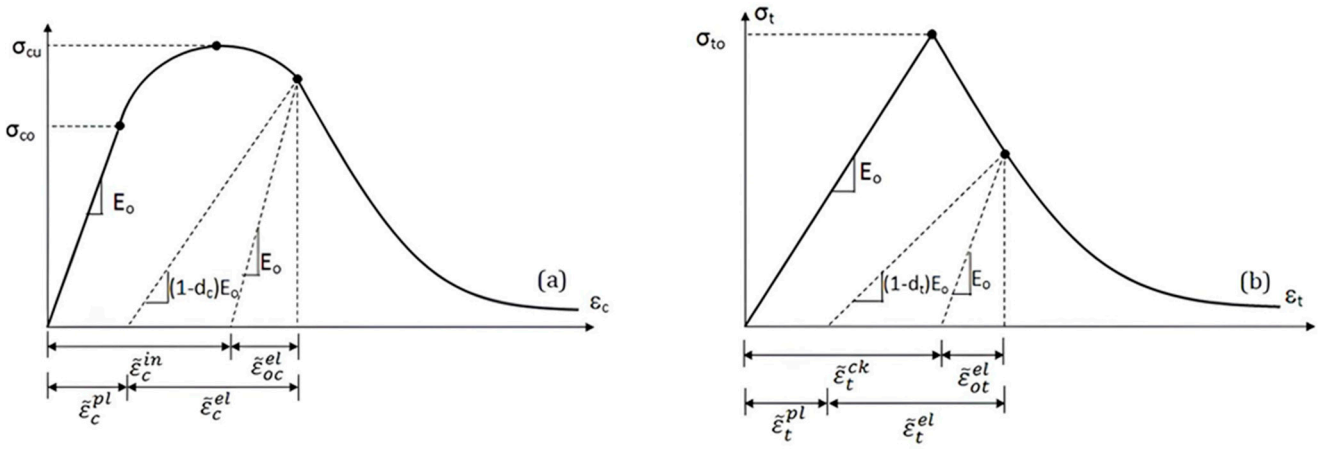


Figure 2. Behavior of concrete under uniaxial compression (**a**) and tension (**b**) [23,24].

When the stress–strain relationship of concrete is examined, it is observed that plastic deformations occur after the tensile and compressive stresses reach their peak values, leading to a reduction in the elastic modulus. This reduction in the elastic modulus is represented by the damage parameters d_t and d_c, which vary between 0 and 1. A value of 0 indicates an undamaged state, while a value of 1 represents maximum damage. The parameter E_0 denotes the initial elastic modulus of the concrete [26].

$\tilde{\varepsilon}_c^{pl}$: plastic strain under compressive loading

$\tilde{\varepsilon}_c^{in}$: inelastic strain under compressive loading

$\varepsilon_t^{\sim pl}$: plastic strain under tensile loading
$\varepsilon_t^{\sim in}$: inelastic strain under tensile loading

The stresses developed under uniaxial tensile and compressive loading are expressed by the following equations (Equations (1) and (2)) [21–23].

$$\sigma_t = (1 - d_t).E_0.(\varepsilon_t - \varepsilon_t^{\sim pl}) \quad (1)$$

$$\sigma_c = (1 - d_c).E_0.(\varepsilon_c - \varepsilon_c^{\sim pl}) \quad (2)$$

The plastic strains developed under uniaxial tensile and compressive loading are expressed by the following equations (Equations (3) and (4)) [21–23].

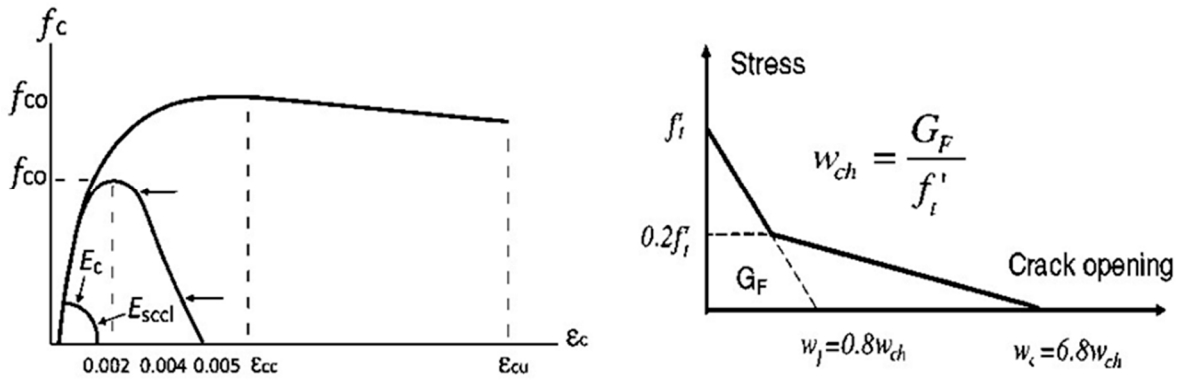
$$\varepsilon_t^{\sim pl} = \varepsilon_t^{\sim ck} - \frac{d_t}{(1 - d_t)} \frac{\sigma_t}{E_0} \quad (3)$$

$$\varepsilon_c^{\sim pl} = \varepsilon_c^{\sim in} - \frac{d_c}{(1 - d_c)} \frac{\sigma_c}{E_0} \quad (4)$$

The influence of tensile stresses on the elastic stiffness of concrete is commonly referred to as tension stiffening in the literature. This mechanism is taken into account in the numerical modeling of cracks that develop along reinforcement due to bond deterioration and slip between concrete and reinforcement. The tension stiffening effect can be represented through the stress–strain relationship of concrete combined with the fracture energy required for crack initiation. The reinforcement–concrete interface behavior is modeled by incorporating the tension stiffening effect into the concrete constitutive model. This approach enables a more accurate representation of load transfer across cracks through reinforcement. Furthermore, it allows the strain-softening behavior of cracked concrete to be captured within the numerical analysis. Therefore, defining the tension stiffening parameter in the Concrete Damaged Plasticity (CDP) model is essential. In ABAQUS, this parameter can be defined either by using a post-peak stress–strain relationship or through a fracture energy-based cracking criterion. Both approaches contribute to a more realistic simulation of the tensile behavior of cracked concrete [25]. Since the compressive and tensile responses of the experimental specimens were not reported, these relationships were established using mathematical models available in the literature. The compressive behavior of concrete was defined using the Mander model [26], while the tensile response was represented by a bilinear relationship, as illustrated in Figure 3b [24]. The crack opening width (wc) is associated with the fracture energy per unit area (GF) required for the initiation and propagation of Mode I cracks in concrete. The Mode I tensile fracture energy of concrete is defined as a function of the concrete compressive strength (fc), as presented in Equation (5) [27]. In this equation, the coefficient Gf_0 depends on the maximum aggregate size (dmax), and the corresponding values are provided in Table 2.

Table 2. Fracture behavior coefficients related to aggregate size.

Maximum Aggregate Size Dmax (mm)	Coefficient Gfo (J/m^2)
8	25
16	30
32	58

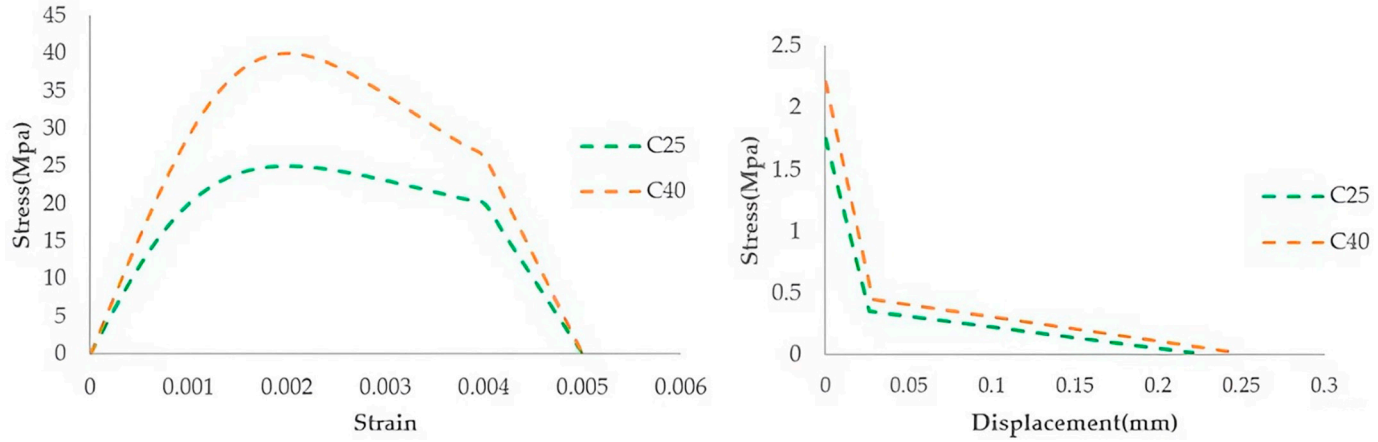


(**a**) (**b**)

Figure 3. Mechanical response of concrete under uniaxial loading expressed through stress–strain curves: (**a**) compressive behavior according to the Mander model, (**b**) idealized bilinear tensile stress–strain model [24,26].

In the finite element model, the uniaxial tensile and compressive stress–strain relationships were established based on the theoretical framework presented in the previous section (Figure 4). In Equation (5), the tensile fracture energy of concrete (G_F) is defined as a function of the concrete compressive strength (f_c) and a coefficient (G_{fo}) related to the maximum aggregate size [27]. In defining the tensile behavior, fracture energy (Gf_0) parameters determined as a function of the maximum aggregate size were utilized, and the corresponding values are provided in Table 2 [28].

$$G_F = G_{fo}\left(\frac{f_c}{10}\right)^{0.7} \quad (5)$$



(**a**) (**b**)

Figure 4. Graphs representing the mechanical behavior of concrete under uniaxial loading: (**a**) compression, (**b**) tension.

3. Verification of Experimental Findings Using Finite Element Analysis

In order to verify the reliability of the numerical model, experimental studies previously reported in the literature were taken as references [29]. In this context, a reinforced concrete deep beam reinforced with GFRP bars was modeled, and the obtained numerical results were compared with the experimental data. The geometrical properties of the specimen are illustrated in Figure 5.

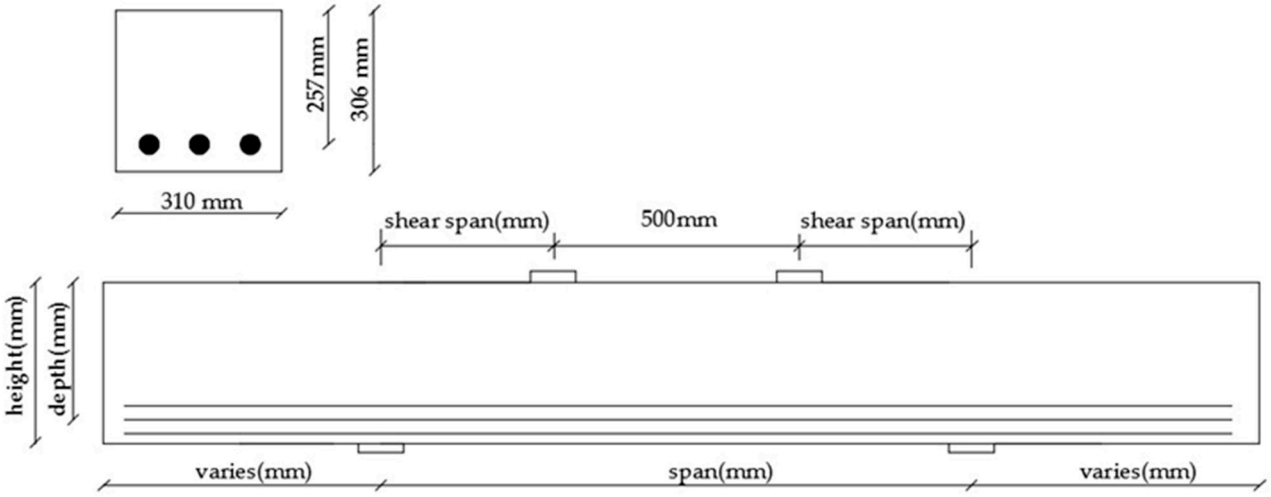


Figure 5. Geometrical properties, reinforcement configuration, and loading conditions of the reference specimen used for the validation of the numerical model [29].

The finite element (FE) model developed in this study was validated using experimental results available in the literature. For this purpose, the A1N specimen from the experimental program conducted by Andermatt and Lubell was selected for the verification study. The A1N specimen represents a reinforced concrete deep beam with a shear span-to-effective depth ratio (a/d) of 1.07, reinforcement ratio of 1.49%, overall beam height of 306 mm, effective depth of 257 mm, shear span of 276 mm, and beam width of 310 mm. In the experimental study, the compressive strength of the concrete was reported as approximately 40.2 MPa [20]. The availability of detailed geometric parameters, material properties, and experimental results in the literature makes this specimen suitable for validating the numerical model. Therefore, the A1N specimen was adopted as the benchmark case to compare the experimental observations with the numerical predictions obtained from the finite element analysis [29].

The mechanical properties of the concrete and GFRP reinforcement bars used in the experimental study are presented in detail in Tables 3 and 4. Within the scope of the experimental program, the compressive strength of the concrete belonging to specimen A1N was determined as 40.2 MPa, while the modulus of elasticity was reported as 23,020 MPa. The ultimate compressive strain of the concrete was given as 0.0027, whereas the strain at the end of the softening curve was reported as 0.0039. In addition, the tensile strength of the concrete was determined as 2.10 MPa and the Poisson's ratio was taken as 0.20. Considering the mechanical properties of the GFRP reinforcement bars used in the experimental study, the #7 GFRP bar has a diameter of 22 mm and a cross-sectional area of 396 mm^2. The rupture stress of the bar was reported as 709 MPa, while the modulus of elasticity was determined as 41,100 MPa and the rupture strain was given as 1.7%. Moreover, the Poisson's ratio of the GFRP reinforcement was reported as 0.26. These mechanical properties were used as fundamental input parameters in the numerical analyses and provided an important basis for the validation of the experimental results.

Table 3. Information related to the data used in the experimental study [29].

Beam No	Ultimate Compressive Strength, MPa	Young's Modulus, MPa	Strain at Ultimate Strength	Strain at End of Softening Curve	Ultimate Tensile Strength, MPa	Poisson's Ratio
A1N	40.2	23,020	0.0027	0.0039	2.10	0.2

Table 4. Mechanical properties of GFRP reinforcement bars used in the experimental study [29].

Bar No	Bar Diameter, mm	Area, mm^2	Failure Stress, (f_{fu}), MPa	Modulus of Elasticity, (E_f), MPa	Rupture Strain, %	Poisson's Ratio (t)
#7	22	396	709	41,100	1.7	0.26

4. Definition of Boundary Conditions and Applied Loading

In the finite element model, the supporting plates were represented using three-dimensional solid elements, and the beam supports were defined as a pin support at the left end and a roller support at the right end. At the pin support, located on the left side of the beam, the nodes along the transverse line at the middle of the bottom surface of the supporting plate were restrained against translation in the x, y, and z directions, while rotations about all axes were allowed. At the roller support on the right side, the nodes located in the same region were restricted only in the vertical direction (y-direction), while translations in the other directions and rotations about all axes were permitted. This support configuration was adopted to represent the simply supported beam condition used in the experimental setup. The load was applied to the model through a loading plate placed on the beam, which acts as an intermediate element to ensure a more uniform distribution of the applied load over the loading region. The loading arrangement and the defined boundary conditions of the finite element model are illustrated in Figure 6.

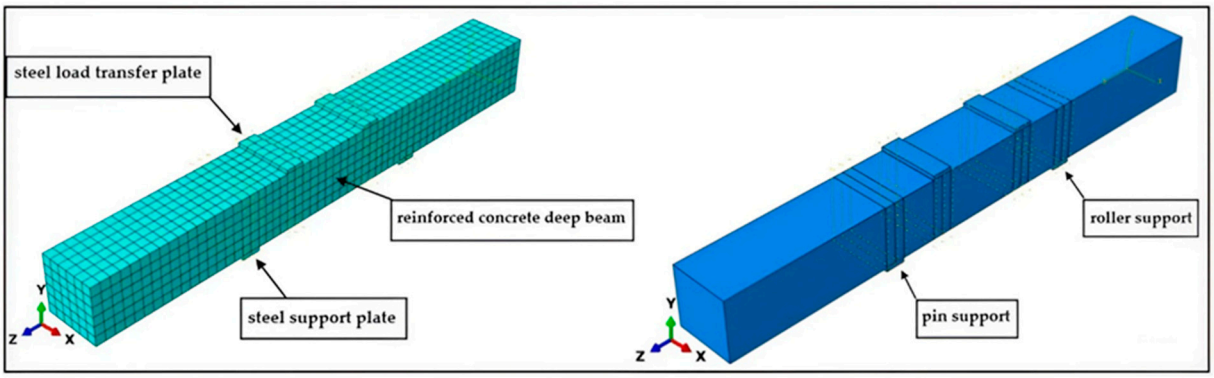


Figure 6. Mesh structure of the finite element model developed for the deep beam.

5. FRP Reinforcement

FRP reinforcements were modeled as isotropic, one-dimensional materials exhibiting linear elastic behavior up to failure [30]. Within this assumption, it was considered that FRP bars do not undergo plastic deformation and fail in a sudden and brittle manner upon reaching their ultimate strength.

6. Beam Modeling and Mesh Sensitivity Analysis

The ABAQUS element library provides a comprehensive geometric modeling capability, allowing different types of elements to be combined within a single model. All elements are based on numerical integration to accurately represent general material behavior. Within this framework, element properties can be defined as general section behaviors, or the cross-sections can be numerically integrated to capture nonlinear responses with high accuracy when required.

Accordingly, during the modeling stage, steel and FRP reinforcements were defined as embedded within the concrete domain, and the reinforcement bars were modeled using two-node three-dimensional truss elements (T3D2—Truss), which are capable of effectively representing axial force transfer. The concrete region, along with the loading

and support plates, was modeled using eight-node linear brick elements with reduced integration (C3D8R), as they can reliably capture nonlinear behavior, contact effects, and large deformations. This element type was selected due to its balanced performance in terms of numerical accuracy and computational efficiency.

To evaluate the reliability of the finite element model, a Mesh Sensitivity Analysis was conducted. Within this framework, the effects of different mesh sizes on the convergence behavior, stability of the results, and computational cost were comparatively investigated. Based on these assessments, a mesh size of 50 mm was adopted in the analyses, as it provides an optimal balance between numerical accuracy and computational performance.

To ensure the accuracy of the numerical results, a structured mesh was adopted for all models. The concrete and steel plates were modeled using 8-node solid elements (C3D8R), while the reinforcement bars were represented by embedded two-node truss elements (T3D2). To evaluate the influence of mesh density on the results, three different mesh sizes (25, 50, and 100 mm) were considered. Based on the comparison of the load–displacement responses, the 50 mm mesh size was found to provide the best balance between accuracy and computational cost; therefore, it was adopted in all analyses. The boundary conditions were defined to represent simply supported beam behavior. As shown in the figure, a pinned support was assigned at the left end, where the nodal translations in all directions (x, y, and z) were restrained while rotations were allowed. At the right end, a roller support was defined, restricting only the vertical displacement (y-direction) while allowing translations in other directions and rotations. The load was applied through steel loading plates, ensuring a more uniform distribution of stresses over the loading region.

The accuracy of the developed finite element model was evaluated by comparing the numerical results obtained using ABAQUS (2022) Standard with the experimental data obtained from reinforced concrete beam specimens. In the validation process, the consistency between the numerical predictions and experimental observations was assessed primarily through load–displacement responses, which represent the fundamental structural behavior of the beam. A comparison between the numerical simulation and experimental results is presented in Figure 7. The comparison indicates that the developed model is capable of capturing the overall structural response of the beam with satisfactory accuracy. The difference between the experimental and numerical results at the maximum load level was found to be approximately 4%, while the discrepancy in the maximum displacement values was within the range of 3–4%. These relatively small differences demonstrate that the proposed finite element model can effectively reproduce both the load-carrying capacity and the deformation characteristics of the reinforced concrete beam.

The load–displacement curves presented in the figure enable a comprehensive comparison between the experimental results and the numerical responses obtained from finite element models with different mesh configurations. Based on the level of agreement between the experimental data and numerical predictions, it is evident that the model employing the M50 mesh configuration provides the most accurate representation of the experimental behavior.

In particular, at moderate and large deformation levels, the M50 model closely follows the experimental trend, demonstrating a high degree of consistency in terms of both load development and ultimate load-carrying capacity (Figure 8). This indicates that the M50 mesh configuration offers an adequate level of discretization for accurately capturing the structural response of the beam.

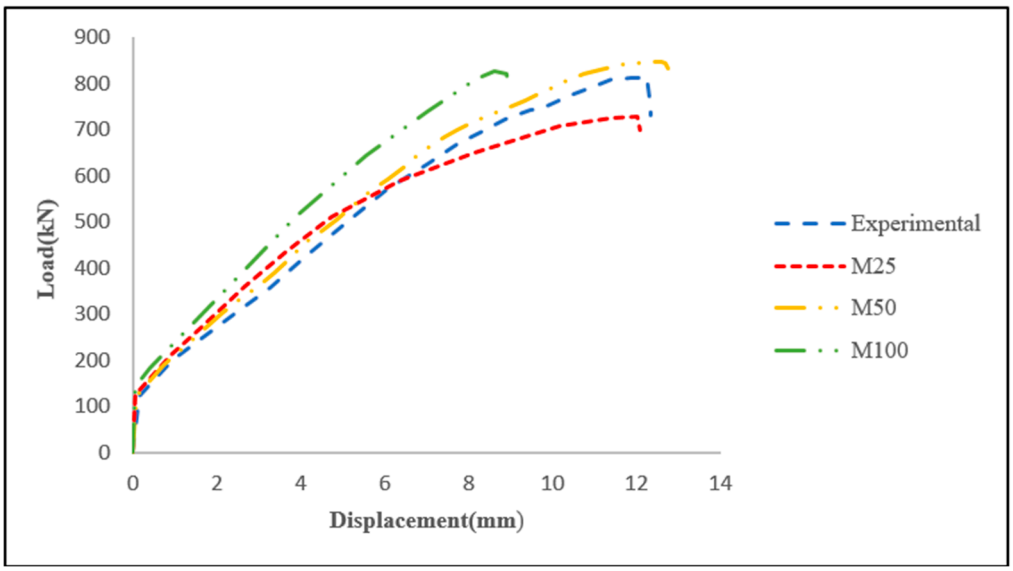


Figure 7. Comparison of load–displacement responses for different mesh sizes (M25, M50, and M100) used in the mesh sensitivity analysis.

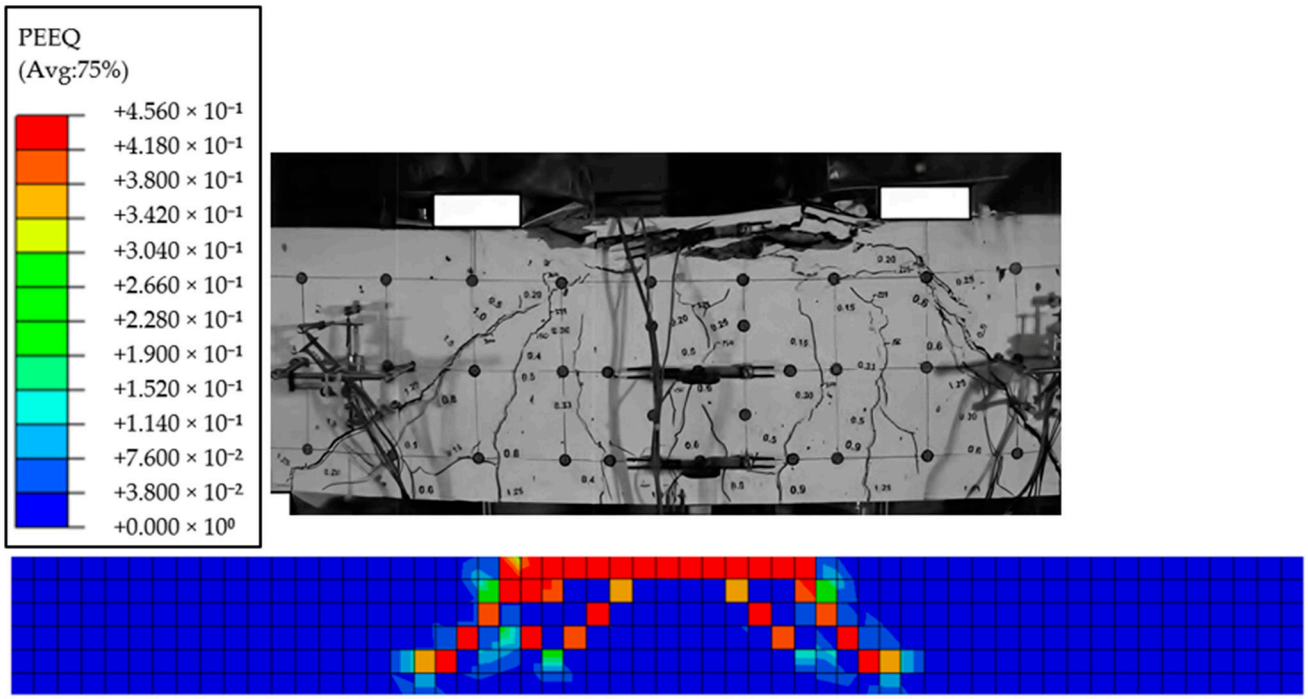


Figure 8. Comparison of experimental and numerical crack distributions for the validation study.

Although the M25 model exhibits a similar overall trend, the predicted maximum load is slightly lower than the experimental value. This discrepancy can be attributed to limitations in representing the stress distribution with finer discretization effects. In contrast, the M100 model shows more pronounced deviations from the experimental response in both load and displacement. Notably, during the initial stages of deformation, the model tends to overestimate the load values, highlighting the sensitivity of the numerical results to mesh density.

Furthermore, the difference between the results obtained using the M50 and M25 mesh configurations is relatively small, indicating that the numerical results are mesh-independent.

Overall, the M50 mesh configuration demonstrates the best agreement with the experimental data, successfully reproducing both the load-carrying capacity and deformation characteristics of the tested specimen. Therefore, it can be concluded that the M50 mesh provides an optimal balance between numerical accuracy and computational efficiency, making it the most suitable choice for the present analysis.

The adequacy and reliability of the developed finite element model were evaluated through both mesh sensitivity analysis and comparison of crack patterns. As presented in Table 5, the M50 mesh configuration provides a balanced agreement with the experimental results in terms of both load (3.12%) and displacement (3.98%), whereas the M25 model shows significant deviation in load prediction and the M100 model fails to accurately capture the deformation behavior. The relatively small differences between the M50 and M25 results further indicate that the numerical solution is mesh-independent. In addition, Figure 8 demonstrates a good correlation between the experimentally observed crack patterns and the numerical damage distributions, confirming that the model is capable of realistically capturing the failure mechanism. Overall, these results confirm that the selected mesh configuration and modeling approach provide accurate and reliable predictions of the overall structural response and local damage behavior.

Table 5. Mesh sensitivity analysis results.

Mesh Size	Max Load(kN)	Max Displacement (mm)	Load Difference (%)	Displacement Difference (%)
100	827.6	8.92	1.75	27.48
50	838.8	12.79	3.12	3.98
25	727.13	12.07	10.60	1.87

7. Parametric Evaluation Study

In this study, a series of deep beam models with different parameters were developed to investigate their structural behavior. GFRP (Glass Fiber Reinforced Polymer) and CFRP (Carbon Fiber Reinforced Polymer) bars were used as longitudinal reinforcement materials. The cross-sectional dimensions of all beams were kept constant with a height of 400 mm (h) and a width of 250 mm (b). The shear span (a) was selected as 400 mm and 500 mm, corresponding to a/d ratios of 1.12 and 1.4, respectively. Two different concrete compressive strength levels were considered in the study: 25 MPa and 40 MPa. The longitudinal tensile reinforcement was arranged as 2Ø12 and 3Ø12 in certain specimens in order to evaluate the influence of reinforcement configuration. In addition, shear reinforcement was kept constant in all beam specimens and provided as Ø6 stirrups with a spacing of 100 mm. The beam specimens were categorized into two main series based on the reinforcement material. The first series consisted of beams reinforced with GFRP bars, while the second series included beams reinforced with CFRP bars. Within each series, variations in the a/d ratio and concrete compressive strength were introduced, resulting in a total of eight different deep beam models. The geometric configurations and reinforcement details of the beam specimens are illustrated in Figure 9 [10,12].

The geometric characteristics and reinforcement configurations of the beam models developed within the scope of the parametric study are presented in Table 6. All beam specimens were designed with dimensions of 400 mm in height (h) and 250 mm in width (b). In the study, the shear span (a) was selected as 400 mm and 500 mm, resulting in a/d ratios of 1.12 and 1.40, respectively. To investigate the influence of reinforcement material, two different series reinforced with GFRP and CFRP bars were considered. In addition, the compressive strength of concrete was taken as 25 MPa and 40 MPa, allowing the effect of concrete strength on beam behavior to be evaluated. The longitudinal tensile reinforcement

was generally arranged as 2Ø12, while in some models 3Ø12 reinforcement was used to examine the effect of reinforcement ratio. To enhance shear capacity and improve shear behavior, Ø10/100 mm steel stirrups were used in all beams. Furthermore, the total beam lengths were determined as 2300 mm and 2500 mm, depending on the selected shear span.

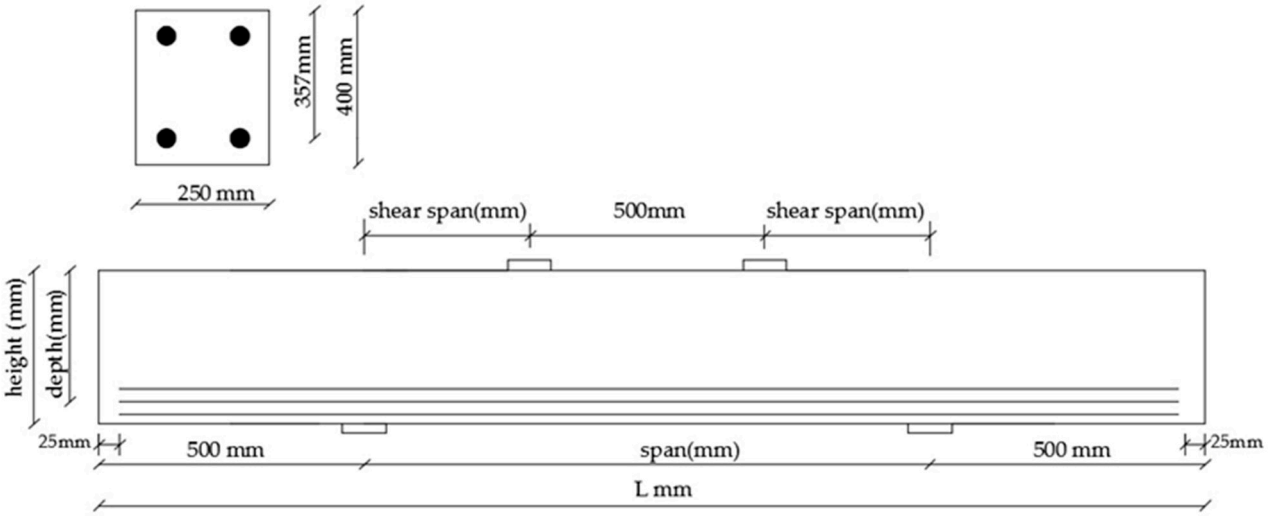


Figure 9. Geometrical properties and reinforcement layout of the deep beams in the case study [10,12].

Table 6. Properties of beam models developed within the scope of the parametric study.

Series	Beam Number	Reinforcing Material	Height (h)	Width (b)	Shear Span (a), mm	a/d	Bottom Bar (mm)	Concrete Strength (MPa)	Stirrups (mm)	L (mm)
1	G-1.12-25	GFRP	400	250	400	1.12	2Ø12	25	Ø10/100	2300
	G-1.4-25	GFRP	400	250	500	1.4	2Ø12	25	Ø10/100	2500
	G-1.12-40#2/3	GFRP	400	250	400	1.12	2Ø12	40	Ø10/100	2300
		GFRP	400	250	400	1.12	3Ø12	40	Ø10/100	2300
	G-1.4-40	GFRP	400	250	500	1.4	2Ø12	40	Ø10/100	2500
2	C-1.12-25	CFRP	400	250	400	1.12	2Ø12	25	Ø10/100	2300
	C-1.4-25	CFRP	400	250	500	1.4	2Ø12	25	Ø10/100	2500
	C-1.12-40#2/3	CFRP	400	250	400	1.12	2Ø12	40	Ø10/100	2300
		CFRP	400	250	400	1.12	3Ø12	40	Ø10/100	2300
	C-1.4-40	CFRP	400	250	500	1.4	2Ø12	40	Ø10/100	2500

The mechanical properties of the reinforcement materials are presented in Table 7 [31]. This table includes fundamental material parameters of reinforcement bars such as yield stress, ultimate tensile strength, modulus of elasticity, and Poisson's ratio. For steel reinforcement, a yield strength of 350 MPa and an elastic modulus of 195 GPa were adopted. Since FRP reinforcements do not exhibit yielding behavior, their material properties were defined based on ultimate tensile strength. Accordingly, the ultimate tensile strengths of GFRP and CFRP bars were taken as 947 MPa and 1890 MPa, respectively. The corresponding elastic modulus values were 45.4 GPa for GFRP and 136.4 GPa for CFRP. These mechanical properties were used in the numerical model to accurately represent the elastic behavior of the reinforcement materials.

Table 7. Mechanical properties of reinforcement bars [31].

Type of the Bar	Dimeter of Bar (mm)	Yield Stress (Mpa)	Ultimate Stress (Mpa)	Modulus of Elasticity (Gpa)	Poisson Ratio
Steel	10	350	-	195	0.3
GFRP	12	-	947	45.4	0.3
CFRP	12	-	1890	136.4	0.3

8. Numerical Analysis Results

After detailed analyses of each deep beam model, the ultimate load capacity and maximum deflection values obtained are systematically presented in this section. In addition, various graphical evaluations are provided to enable a more comprehensive assessment of the effects of the investigated parameters on the structural behavior of the beams.

Within the scope of the study, deep beam models with different reinforcement types, concrete compressive strengths, a/d ratios, and tensile reinforcement arrangements were developed, and detailed numerical analyses were performed for each model. The ultimate load capacity and mid-span deflection values obtained from these analyses are systematically organized and presented in tabular form for comparison.

Furthermore, graphical comparisons were prepared in order to more clearly illustrate the influence of the investigated parameters on the structural behavior of the deep beams. The presented tables and graphs allow the behavior of the different beam models to be examined from both visual and numerical perspectives, thereby providing a clearer understanding of the interactions between the analyzed parameters and their influence on the structural performance of the deep beams.

9. Load–Deformation Response

In this section, the load–deformation responses of deep beams are examined, and the effects of variations in reinforcement type (GFRP–CFRP), a/d ratio, concrete compressive strength, and tensile reinforcement ratio on the stiffness, deflection, and load-carrying capacity of the beams are evaluated through graphical and numerical results. The figure presents the load–displacement behavior of GFRP-reinforced deep beams with different a/d ratios. The load–displacement curves of specimens G-1.12–25 and G-1.4–25 are compared (Figure 10). Examination of the curves indicates that the beam with the smaller a/d ratio exhibits a higher load-carrying capacity. At similar displacement levels, this beam is able to carry higher loads and therefore demonstrates greater stiffness. In contrast, the beam with the larger a/d ratio shows a more pronounced increase in displacement. This behavior can be attributed to the reduction in the effectiveness of the arch mechanism as the a/d ratio increases, causing the beam behavior to be governed more by flexure–shear interaction. Overall, the results indicate that the a/d ratio is an important parameter influencing the stiffness and load–displacement behavior of deep beams.

The ultimate load capacity results presented in Figure 11 clearly demonstrate that the load-carrying capacity of GFRP-reinforced deep beams is governed by the combined effects of the shear span-to-depth ratio (a/d), concrete compressive strength, and longitudinal reinforcement ratio. In deep beams, lower a/d ratios promote the development of an arching action, where load transfer occurs predominantly through diagonal compression struts rather than flexural mechanisms, leading to a significant enhancement in shear capacity. Compared to the reference specimen G-1.4-25 (423 kN), a substantial increase of approximately 64.5% was observed in the G-1.4-40 (696 kN) specimen, where only the concrete strength was increased. This indicates that even at a constant a/d ratio, the

capacity of deep beams is primarily governed by the compressive strength of the concrete strut. On the other hand, for the G-1.12-25 (582 kN) specimen, where the a/d ratio was reduced (1.4 → 1.12) and the reinforcement ratio was increased, an approximate 37.6% improvement in load capacity was achieved compared to the reference specimen. This result highlights that a lower a/d ratio enhances the arching mechanism, resulting in a shorter and more efficient load transfer path. However, the observed improvement cannot be attributed solely to geometric effects, as it is also influenced by the increased reinforcement ratio, which enhances the capacity of the tension ties. The highest load capacity was obtained for the G-1.12-40/2 (756 kN) specimen, which combines a low a/d ratio with high concrete strength and an increased reinforcement ratio. When compared to G-1.4-40, which has the same concrete strength, the capacity increase of approximately 8.6% indicates that the improvement is not solely due to concrete strength but also to the combined mechanical contribution of reduced a/d ratio and enhanced reinforcement ratio. From a deep beam behavior perspective, the diagonal compression strut formed at low a/d ratios must be effectively balanced by sufficient tension ties. Therefore, the increases in load capacity observed in Figure 11 are not only governed by the compressive strength of concrete but also by the stabilizing effect of the longitudinal reinforcement within the strut–tie mechanism.

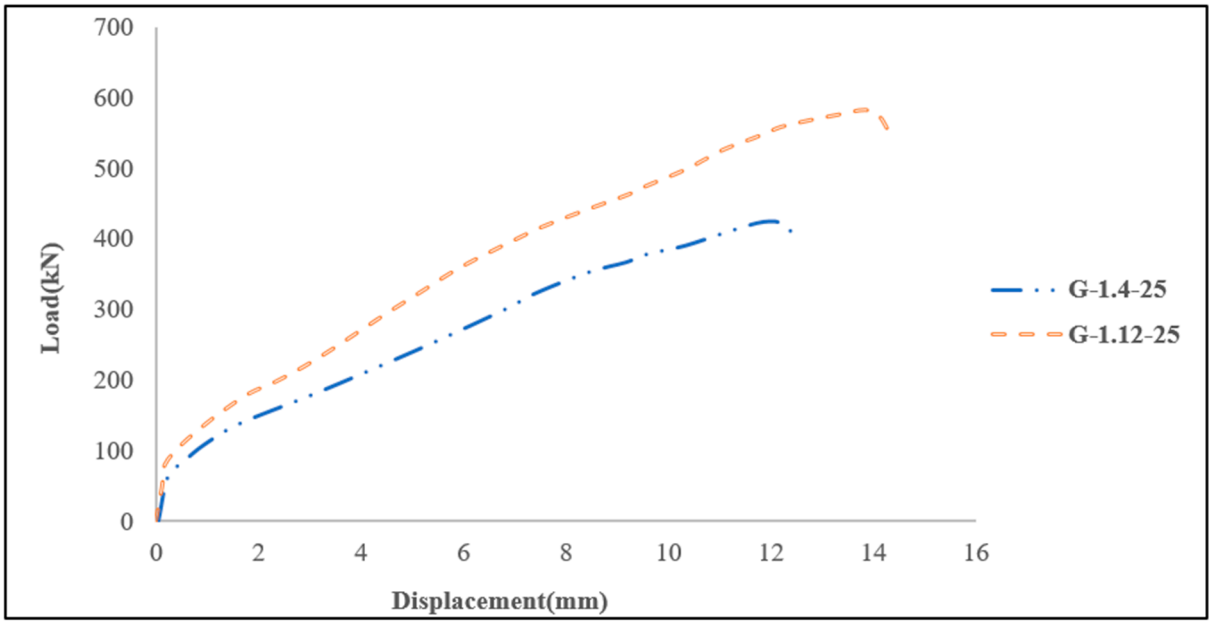


Figure 10. Comparison of load–displacement curves of GFRP reinforced deep beams with different a/d ratio.

The load–displacement curves presented in Figure 12 clearly indicate that the specimens exhibit distinct differences in both load-carrying capacity and deformation behavior depending on the governing parameters. The reference specimen G-1.4-25 shows the lowest performance, with an ultimate load of approximately 423 kN and a displacement of 13 mm. With the reduction in the a/d ratio, the G-1.12-25 specimen reaches a maximum load of about 582 kN (a 37.6% increase), while the ultimate displacement increases to 15 mm, indicating an improvement in deformation capacity. For the G-1.4-40 specimen, where the concrete strength is increased, the maximum load reaches 696 kN (a 64.5% increase), with a corresponding displacement of 16 mm. This behavior is particularly evident in the mid- and post-cracking stages, where higher load levels are sustained. The highest performance is observed in the G-1.12-40/2 and G-1.12-40/3 specimens. These specimens achieve maximum loads of 756 kN and 808 kN, with ultimate displacements of 17 mm

and 18 mm, respectively. Notably, the G-1.12-40/3 specimen exhibits an approximately 91% increase in load capacity compared to the reference specimen. Examination of the curve slopes shows that the initial stiffness is similar for all specimens, whereas significant divergence occurs in the post-cracking region. Furthermore, considering the area under the curves, the energy absorption capacity is notably higher in the G-1.12-40/2 and G-1.12-40/3 specimens. Overall, reducing the a/d ratio, increasing concrete strength, and enhancing the reinforcement ratio collectively improve the load–displacement response, leading to significant increases in both ultimate load capacity and deformation and energy absorption capacities.

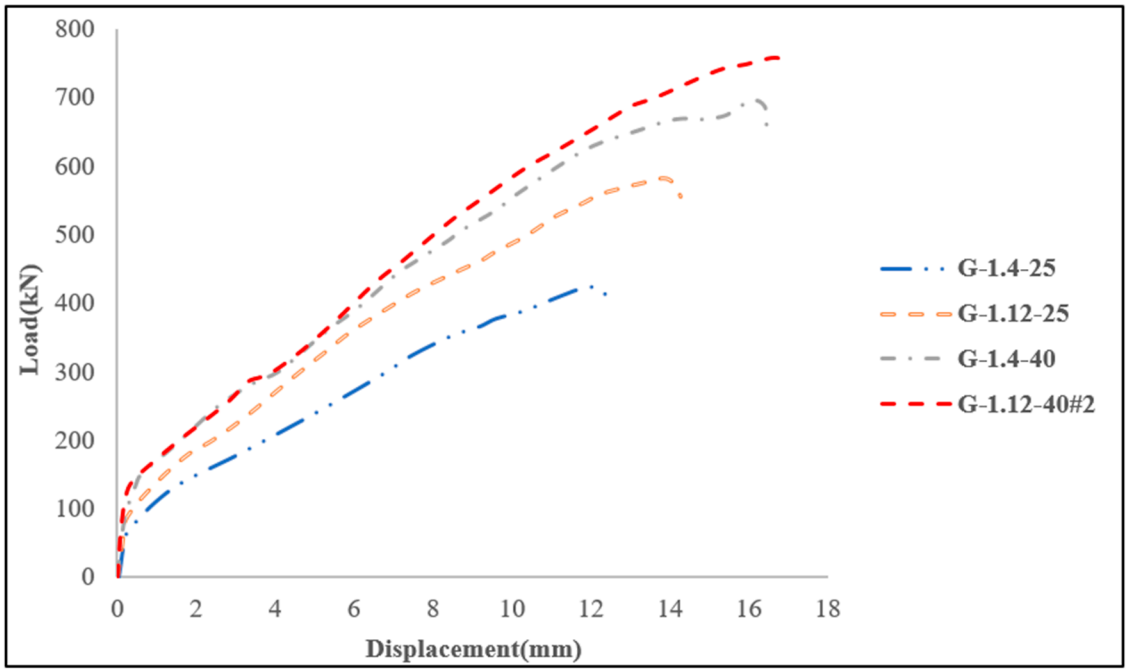


Figure 11. Comparison of load–displacement curves of GFRP reinforced deep beams with different concrete compressive strengths and a/d ratio.

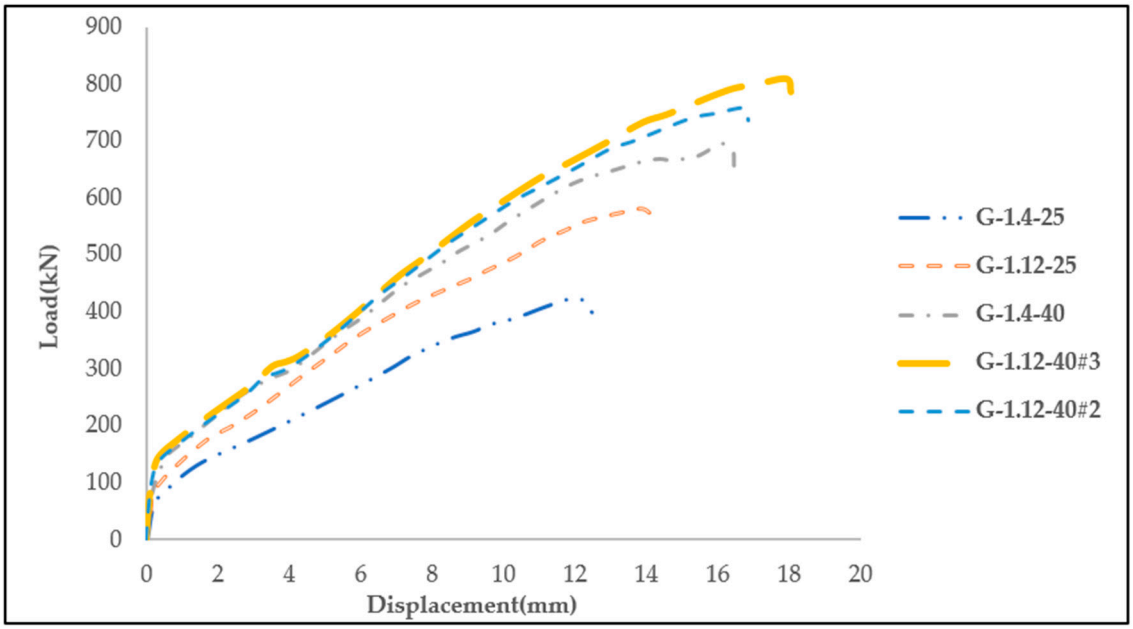


Figure 12. Comparison of load–displacement responses of GFRP-reinforced deep beams with different parameters.

The load–displacement curves presented in Figure 13 provide a direct comparative evaluation of the structural performance of GFRP- and CFRP-reinforced deep beams. Examination of the curves clearly indicates that CFRP-reinforced specimens achieve higher load capacities than their GFRP counterparts across all parameter levels. Under similar conditions in terms of a/d ratio and other parameters, the C-1.12-25 specimen reaches approximately 700 kN, whereas the G-1.12-25 specimen remains around 580 kN. This indicates that CFRP reinforcement provides approximately 20–25% higher load-carrying capacity compared to GFRP. A similar trend is observed for specimens with a/d = 1.4, where the C-1.4-25 specimen (approximately 630 kN) exhibits about 48% higher capacity than the G-1.4-25 specimen (approximately 423 kN). In terms of deformation capacity, GFRP-reinforced specimens exhibit higher displacement values. The ultimate displacements for the GFRP series range between 13–18 mm, whereas those of the CFRP series remain within 8–12 mm. This behavior can be attributed to the higher elastic modulus of CFRP reinforcement, which results in a stiffer structural response, while GFRP allows greater deformation capacity. Analysis of the curve slopes further supports this observation, as CFRP-reinforced specimens exhibit steeper slopes in both the initial and intermediate loading stages, indicating higher stiffness. In contrast, GFRP-reinforced specimens display more gradual slopes and sustain larger displacements.

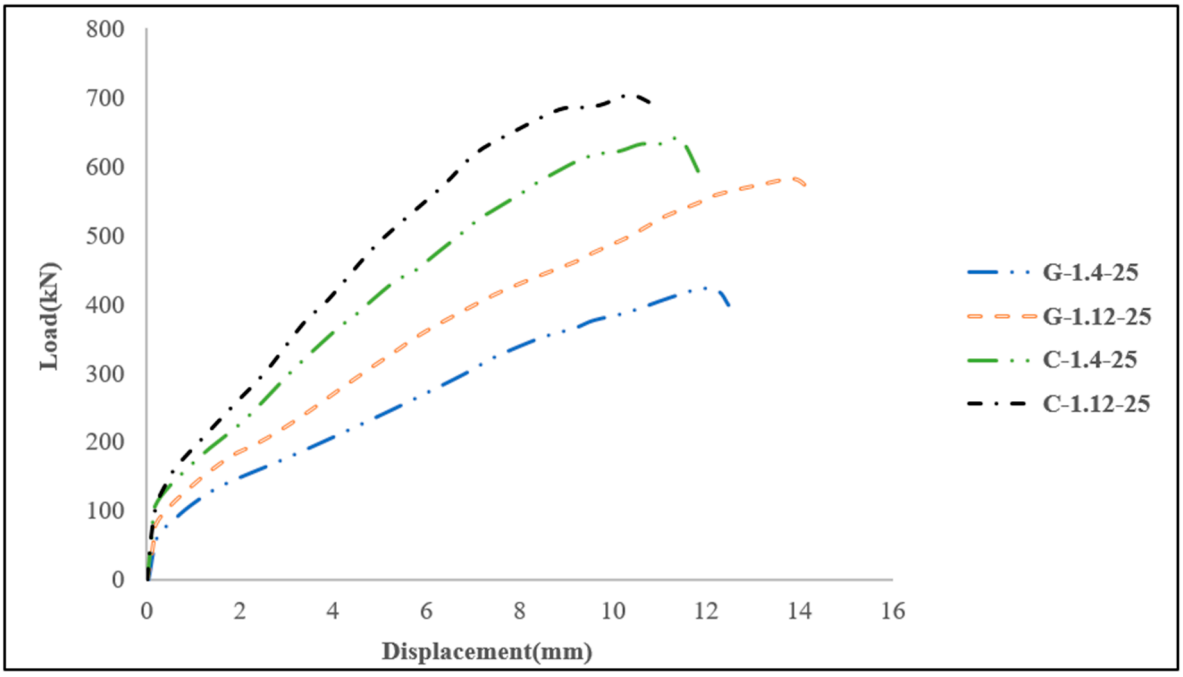


Figure 13. Comparison of load–displacement curves of deep beams reinforced with different reinforcement types (GFRP and CFRP) and a/d ratios.

From an energy absorption perspective, the area under the load–displacement curves is generally larger for GFRP-reinforced specimens, indicating superior energy absorption capacity. This suggests that GFRP-reinforced systems may offer advantages under impact or dynamic loading conditions. Overall, the results presented in Figure 13 demonstrate that CFRP reinforcement enhances load-carrying capacity and stiffness due to its higher elastic modulus and tensile strength, whereas GFRP reinforcement provides greater deformation and energy absorption capacity. Accordingly, CFRP reinforcement appears to be more suitable for applications requiring higher load capacity, while GFRP reinforcement offers advantages in systems where greater deformation capacity and energy dissipation are desired.

The load–displacement curves presented in Figure 14 provide a comparative evaluation of the behavior of GFRP- and CFRP-reinforced deep beams, particularly at a higher concrete strength level (f'c ≈ 40 MPa). Examination of the curves shows that CFRP-reinforced specimens reach significantly higher load levels than GFRP specimens throughout the entire displacement range. Within the GFRP series, the G-1.4-40 specimen reaches an ultimate load of approximately 696 kN, while a gradual increase in capacity is observed in the G-1.12-40/2 (approximately 756 kN) and G-1.12-40/3 (approximately 808 kN) specimens due to the reduction in a/d ratio and the increase in reinforcement ratio. In contrast, the corresponding CFRP-reinforced specimens exhibit substantially higher capacities under the same parameter combinations. Specifically, the C-1.4-40 specimen (approximately 904 kN) shows about 30% higher capacity than its GFRP counterpart, whereas the C-1.12-40/2 (approximately 1082 kN) and particularly the C-1.12-40/3 (approximately 1249 kN) specimens demonstrate even more pronounced differences. The C-1.12-40/3 specimen provides up to approximately 80% higher capacity compared to the reference GFRP specimen G-1.4-40. This finding clearly indicates that the type of reinforcement alone plays a highly decisive role in the behavior of deep beams. In terms of deformation capacity, CFRP-reinforced specimens reach their maximum load at relatively lower displacement levels, whereas GFRP specimens continue to sustain load at higher displacement levels. This behavior suggests that CFRP reinforcement leads to a stiffer structural response due to its higher elastic modulus, while GFRP reinforcement exhibits a more ductile deformation characteristic. Analysis of the curve slopes further confirms that CFRP-reinforced specimens have steeper slopes in the initial and intermediate loading stages, indicating higher stiffness. In contrast, GFRP specimens display more gradual and flatter curves, which are associated with greater deformation capacity.

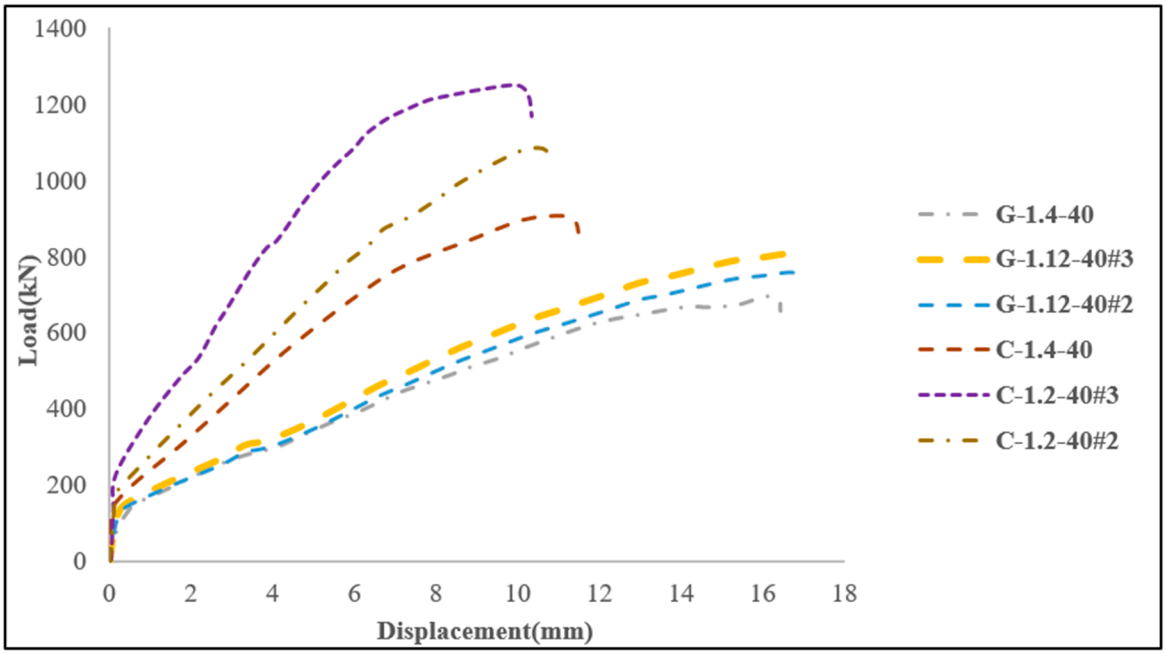


Figure 14. Comparison of load–displacement curves of deep beams with different reinforcement types (GFRP and CFRP) and a/d ratios.

10. Evaluation of Energy Absorption Capacity

In this section, the energy absorption capacities of GFRP-reinforced deep beams were analyzed based on the area under the load–displacement curves, and the effects of key parameters on this capacity were investigated. The energy absorption capacity was calculated through numerical integration of the area under the load–displacement curve.

In this context, the area under the curve was determined using the trapezoidal method based on the load–displacement data obtained from the finite element analyses. In the calculations, a linear variation between consecutive data points was assumed, and the total energy absorption capacity was obtained by summing the incremental areas. This approach reliably represents the energy absorbed by the structure during the deformation process under loading and is widely adopted in the literature.

Figure 15 shows that the energy absorption capacities of GFRP-reinforced deep beams are significantly influenced by changes in the a/d ratio, concrete compressive strength, and tensile reinforcement ratio.

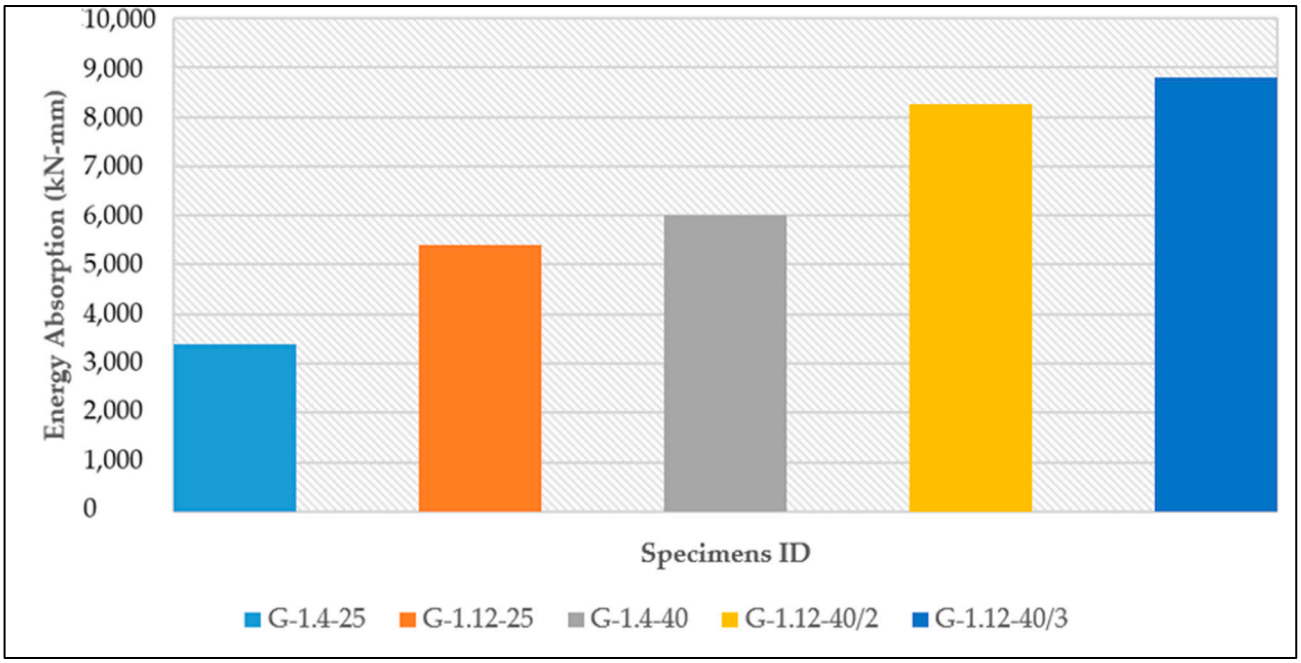


Figure 15. Comparative analysis of the energy absorption capacities of GFRP-reinforced deep beams under varying a/d ratios and concrete compressive strengths.

The energy absorption results obtained from Figures 15 and 16 clearly demonstrate the influence of key parameters on the structural performance of both GFRP- and CFRP-reinforced deep beams. For GFRP-reinforced specimens, reducing the a/d ratio from 1.4 to 1.12 (G-1.4-25 to G-1.12-25) increases the energy absorption capacity from 3390 kN·mm to 5394 kN·mm, corresponding to an increase of approximately 59%. This significant improvement is attributed to the enhanced arching action, which enables more efficient load transfer through diagonal compression struts.

The effect of concrete compressive strength is also pronounced. Increasing the concrete strength from 25 MPa to 40 MPa (G-1.4-25 to G-1.4-40) results in an increase in energy absorption from 3390 kN·mm to 6000 kN·mm (approximately 77%). This behavior can be explained by the increased capacity of the compression struts under higher-strength concrete. Furthermore, increasing the tensile reinforcement ratio leads to additional improvements, where the energy absorption increases from 6000 kN·mm (G-1.4-40) to 8246 kN·mm and 9436 kN·mm for the G-1.12-40/2 and G-1.12-40/3 specimens, respectively. This corresponds to increases of approximately 37% and 57%, indicating the enhanced contribution of the tension zone at higher reinforcement ratios.

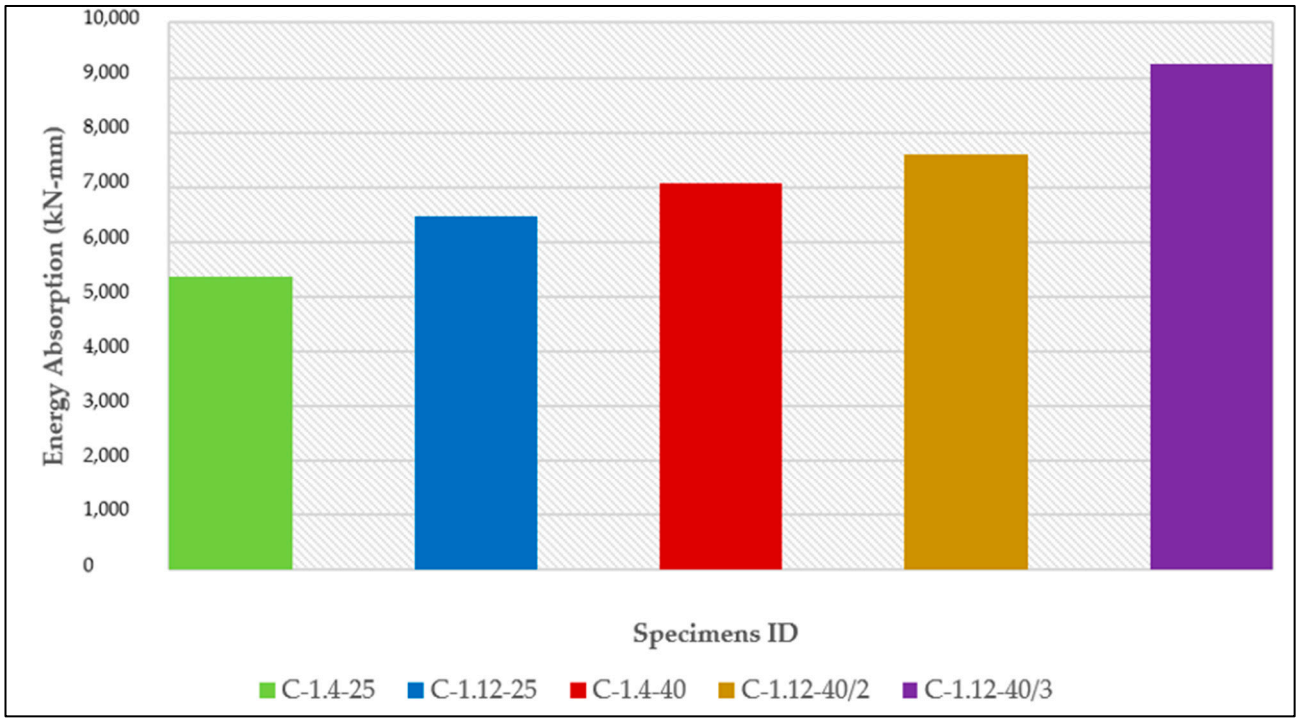


Figure 16. Comparison of energy absorption capacities of CFRP-reinforced deep beams with different a/d ratios and concrete strengths.

A similar trend is observed for CFRP-reinforced specimens; however, the magnitude of increase differs. Reducing the a/d ratio (C-1.4-25 to C-1.12-25) increases the energy absorption capacity from 5394 kN·mm to 6446 kN·mm (approximately 19.5%). Increasing the concrete strength (C-1.4-25 to C-1.4-40) leads to an increase to 7079 kN·mm (approximately 31.2%). Further increases in reinforcement ratio result in energy absorption values of 7602 kN·mm and 9262 kN·mm for the C-1.12-40/2 and C-1.12-40/3 specimens, respectively, corresponding to additional increases of approximately 7% and 22%. These results indicate that CFRP-reinforced systems exhibit a more stiffness-dominated response, where increases in energy absorption are primarily governed by higher load levels rather than deformation capacity.

When the two reinforcement types are compared under similar parameter conditions, CFRP-reinforced deep beams consistently exhibit higher energy absorption capacities than GFRP-reinforced beams. For instance, under the reference condition (a/d = 1.4, f'c = 25 MPa), CFRP beams show approximately 59% higher energy absorption (5394 vs. 3390 kN·mm). However, the relative increase in GFRP systems is more pronounced with parameter changes, highlighting their greater sensitivity to geometric and material variations. This behavior can be attributed to the lower elastic modulus of GFRP, which allows for larger deformations and greater energy dissipation.

Overall, the results confirm that the a/d ratio, concrete compressive strength, tensile reinforcement ratio, and reinforcement type significantly influence the energy absorption capacity of deep beams. Specifically, reduced a/d ratios enhance arching action, increased concrete strength improves compression strut capacity, and higher reinforcement ratios strengthen the tension zone, collectively leading to improved energy absorption performance.

11. Maximum Load Capacity

The results presented in Figures 17 and 18 clearly demonstrate the influence of key parameters on the maximum load capacity of GFRP- and CFRP-reinforced deep beams.

For GFRP-reinforced specimens (Figure 17), reducing the a/d ratio from 1.4 to 1.12 leads to a significant increase in load capacity of approximately 37.6%. In contrast, the same reduction in CFRP-reinforced specimens (Figure 18) results in a more limited increase of about 10.0%, indicating that GFRP-reinforced beams are more sensitive to variations in the a/d ratio due to their lower stiffness and greater dependence on arching action.

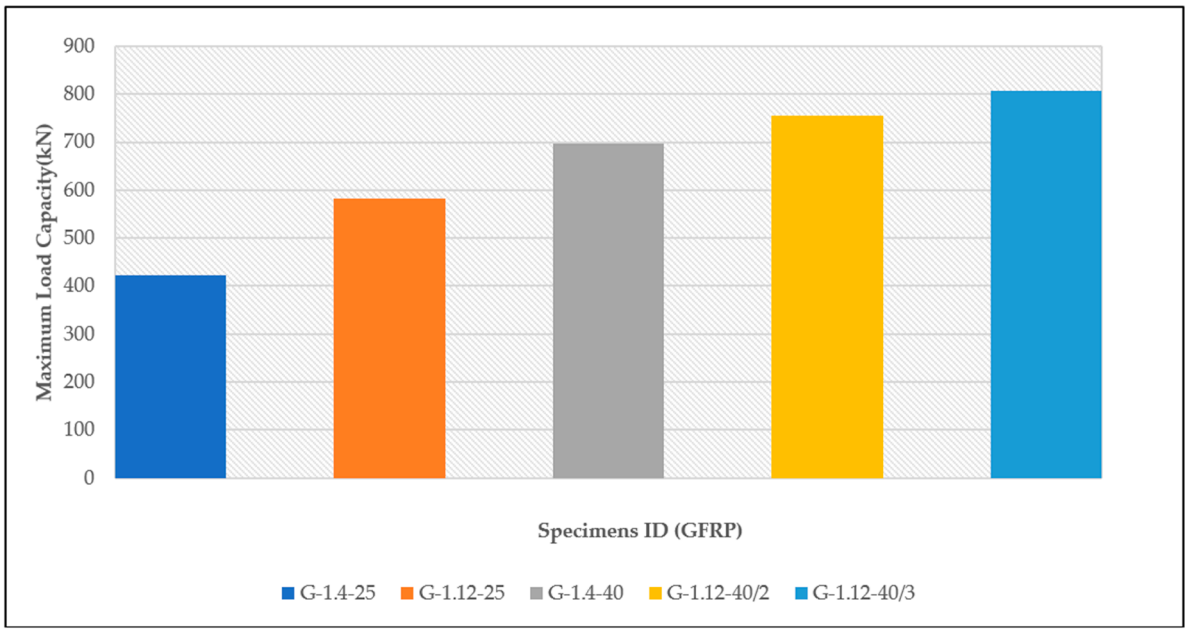


Figure 17. Effect of different parameters on the maximum load capacity of GFRP-reinforced deep beams.

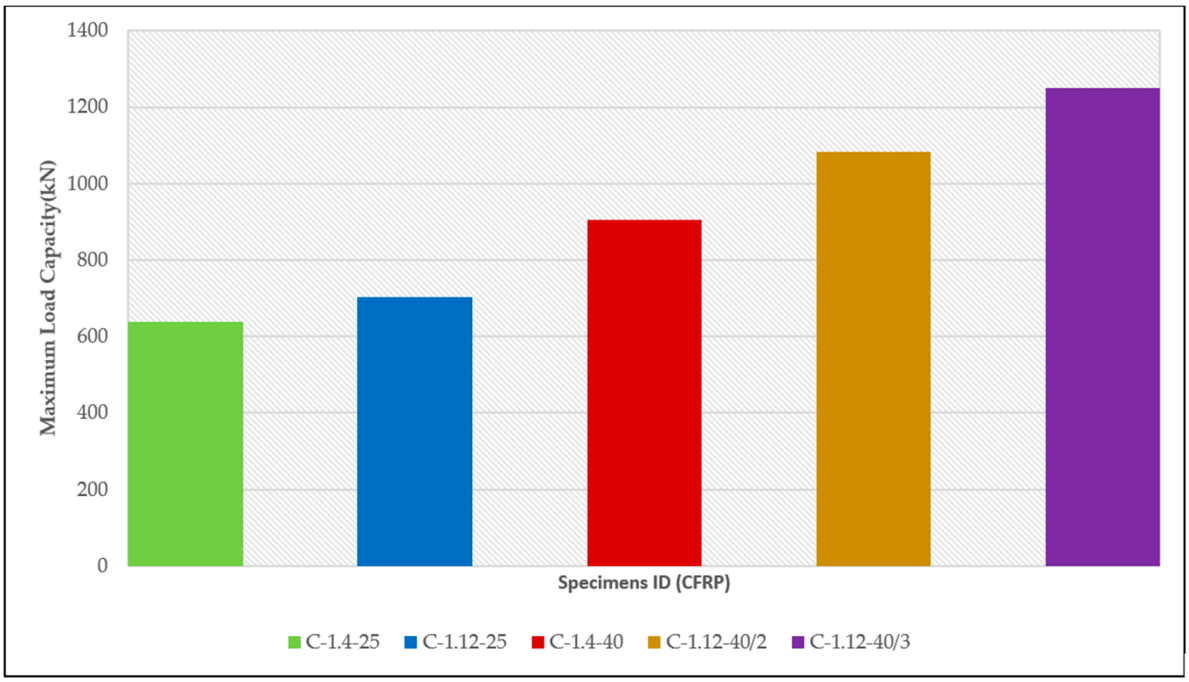


Figure 18. Effect of different parameters on the maximum load capacity of CFRP-reinforced deep beams.

The effect of concrete compressive strength is pronounced in both systems. Increasing the concrete strength from 25 MPa to 40 MPa results in a substantial increase in load capacity, reaching approximately 64.5% for GFRP-reinforced beams and 41.7% for CFRP-

reinforced beams. This behavior can be attributed to the enhanced capacity of the diagonal compression strut, which plays a dominant role in load transfer in deep beams.

When the tensile reinforcement ratio is increased, GFRP-reinforced specimens exhibit relatively limited improvements in load capacity (approximately 7–9%), whereas CFRP-reinforced specimens show more significant increases, ranging between 15% and 20%. This difference highlights the more effective contribution of CFRP reinforcement due to its higher elastic modulus and tensile strength, which enhances stiffness and load-carrying capacity.

A direct comparison between the two reinforcement types shows that CFRP-reinforced deep beams consistently achieve higher maximum load capacities than GFRP-reinforced beams under similar conditions. The difference ranges from approximately 20% to 55% and becomes more pronounced with increasing concrete strength and reinforcement ratio. Overall, these results indicate that while GFRP systems are more sensitive to geometric parameters, CFRP systems provide superior strength performance due to their stiffness-dominated behavior.

12. Ultimate Displacement

The ultimate displacement results presented in Figures 19 and 20 reveal distinct deformation trends between GFRP- and CFRP-reinforced deep beams under varying parameters. For GFRP-reinforced specimens, the ultimate displacement increases progressively with decreasing a/d ratio, increasing concrete strength, and higher reinforcement ratios. Specifically, reducing the a/d ratio from 1.4 to 1.12 leads to an increase of approximately 15%, while increasing concrete strength results in a further improvement of about 23%. Additional increases in reinforcement ratio contribute to a gradual rise in displacement capacity, reaching up to 18 mm. This behavior indicates that GFRP-reinforced systems benefit from the combined influence of geometric and material parameters, resulting in enhanced deformation capacity due to their relatively lower elastic modulus and more flexible response.

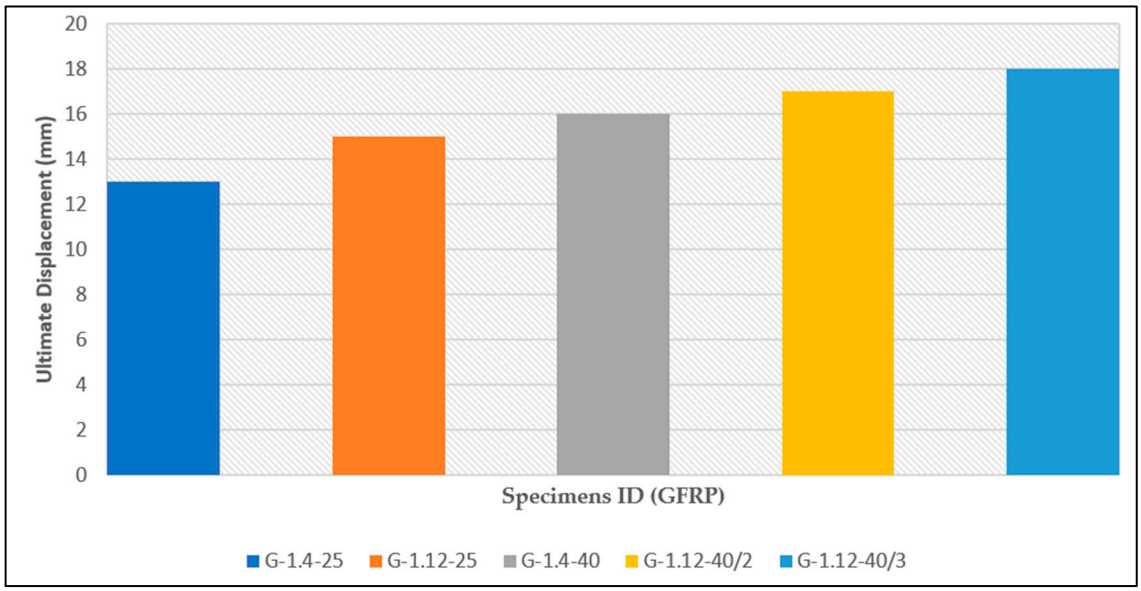


Figure 19. Ultimate displacement values of GFRP-reinforced deep beams under different parameter variations.

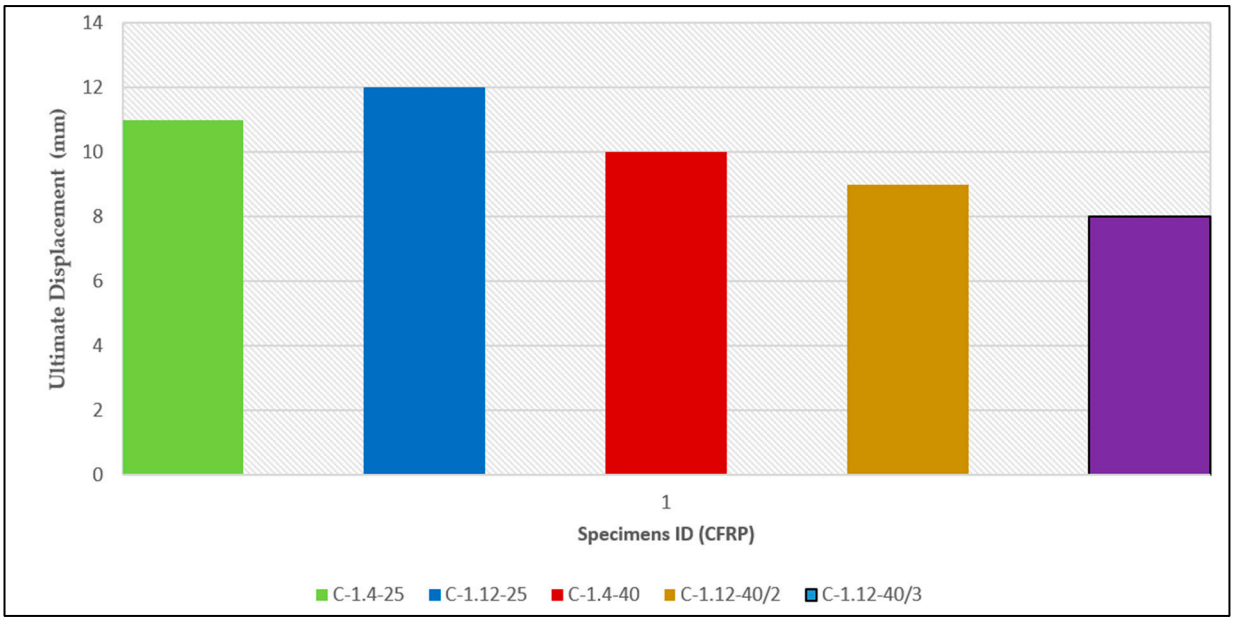


Figure 20. Ultimate displacement values of CFRP-reinforced deep beams under different parameter variations.

In contrast, CFRP-reinforced specimens exhibit an opposite trend. Although a slight increase in displacement is observed with the reduction in the a/d ratio (approximately 9%), increasing concrete strength and reinforcement ratio leads to a reduction in ultimate displacement. This decrease is associated with the higher stiffness of CFRP reinforcement, which restricts deformation and promotes a more brittle structural response. As a result, the ultimate displacement decreases to approximately 8–10 mm under higher parameter levels.

A direct comparison between the two reinforcement types shows that GFRP-reinforced deep beams consistently achieve higher ultimate displacement values than CFRP-reinforced beams. This difference becomes more pronounced with increasing concrete strength and reinforcement ratio. The results clearly demonstrate that the reinforcement type plays a critical role in controlling the deformation capacity, where GFRP provides a more ductile response, while CFRP leads to stiffness-dominated behavior.

13. Parameters Influencing Shear Capacity

In this section, the trends in shear capacity were investigated in terms of the a/d ratio, tensile reinforcement ratio (ρ), concrete compressive strength (f_c'), and reinforcement type (GFRP and CFRP). To ensure consistency in the parametric comparisons, the peak shear stress was normalized with respect to f_c', as given in Equation (6) [29,32]:

$$v = \frac{P_{max}}{2b_w d f_c'} \tag{6}$$

13.1. Effect of a/d Ratio and Reinforcement Ratio on Shear Capacity

Figure 21 illustrates the variation in shear capacity with respect to the a/d ratio and tensile reinforcement ratio (ρ) for both GFRP- and CFRP-reinforced deep beams. The results clearly indicate that the a/d ratio is one of the most influential parameters governing shear behavior.



(**a**) (**b**)

Figure 21. Variation in normalized shear capacity with respect to (**a**) a/d ratio at 25 MPa concrete strength and (**b**) tensile reinforcement ratio at 40 MPa for GFRP- and CFRP-reinforced deep beams.

Reducing the a/d ratio from 1.40 to 1.12 led to a significant increase in shear capacity for all specimens. This increase reached approximately 38% in GFRP-reinforced beams, while it ranged between 10–20% in CFRP-reinforced beams. This indicates that the effect of decreasing a/d becomes more pronounced in beams reinforced with higher-stiffness materials.

The influence of tensile reinforcement ratio, although less dominant, remains notable. Increasing the reinforcement ratio resulted in an improvement of approximately 6% in GFRP-reinforced beams and about 15% in CFRP-reinforced beams.

Overall, the findings demonstrate that the reduction in a/d significantly enhances shear capacity due to the development of a stronger arch action mechanism. In contrast, the contribution of increasing the reinforcement ratio remains secondary. Additionally, CFRP-reinforced beams exhibit higher performance gains compared to GFRP-reinforced beams.

13.2. Effect of Concrete Compressive Strength on Shear Capacity

Figure 22 illustrates the influence of concrete compressive strength on the normalized shear capacity of GFRP- and CFRP-reinforced deep beams. The results indicate that increasing concrete strength does not necessarily lead to an improvement in shear capacity; on the contrary, it may result in a reduction under certain conditions.

For GFRP-reinforced beams at a/d = 1.12, increasing the concrete strength from 25 MPa to 40 MPa led to a decrease in normalized shear capacity of approximately 19%. In contrast, for a/d = 1.40, the change remained limited, with a slight decrease of about 1–2%. This suggests that the influence of concrete strength becomes more pronounced at lower a/d ratios.

A different trend is observed in CFRP-reinforced beams. At a/d = 1.12, increasing the concrete strength resulted in only a minor reduction of approximately 4% in normalized shear capacity, whereas at a/d = 1.40, the reduction became more significant, reaching approximately 11%. These findings highlight that the effect of concrete strength on shear behavior is dependent on both the a/d ratio and the type of reinforcement.

Overall, the results demonstrate that an increase in concrete compressive strength tends to reduce the normalized shear capacity. This behavior can be attributed to the more brittle cracking characteristics of higher-strength concrete, which promotes rapid crack propagation and limits stress redistribution. Particularly in deep beams where arch action

governs load transfer, the reduced deformability of high-strength concrete may lead to stress localization and, consequently, a decrease in normalized shear capacity.

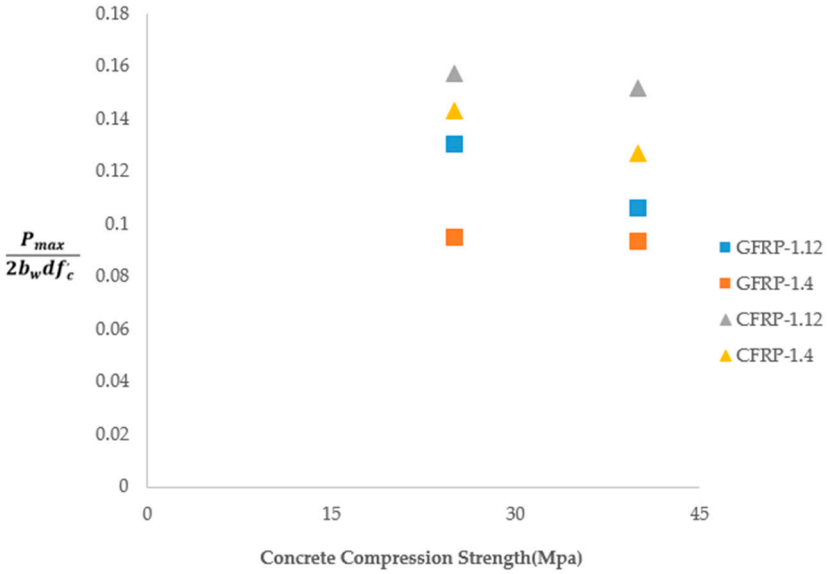


Figure 22. Variation in normalized shear capacity with respect to concrete compressive strength for GFRP- and CFRP-reinforced deep beams at different a/d ratios.

14. Conclusions

In this study, the nonlinear behavior of reinforced concrete deep beams reinforced with GFRP and CFRP bars was investigated considering key parameters such as the a/d ratio, concrete compressive strength, tensile reinforcement ratio, and reinforcement type. The results indicate that deep beam behavior is governed by the interaction of geometric, material, and reinforcement characteristics.

1. The results clearly indicate that the a/d ratio is one of the most influential parameters governing the shear behavior of deep beams. Reducing the a/d ratio from 1.40 to 1.12 led to a significant increase in shear capacity, particularly for GFRP-reinforced beams, where the increase reached approximately 35–40%. This enhancement is attributed to the more effective development of the arch action mechanism, enabling efficient load transfer through diagonal compression struts.

2. The type of reinforcement was found to have a pronounced effect on the structural response. CFRP-reinforced beams consistently exhibited higher load-carrying capacities than GFRP-reinforced beams, with increases ranging between approximately 20% and 55%. In contrast, GFRP-reinforced beams demonstrated higher ultimate displacement and deformation capacity, reflecting a more ductile structural response.

3. Increasing the concrete compressive strength did not always result in an improvement in normalized shear capacity. Particularly at lower a/d ratios (a/d = 1.12), increasing the concrete strength from 25 MPa to 40 MPa led to a reduction in normalized shear capacity. This behavior is associated with the more brittle cracking characteristics of higher-strength concrete, which promotes stress localization and limits stress redistribution.

4. The tensile reinforcement ratio contributed to improvements in both shear capacity and energy absorption; however, its influence remained secondary compared to the a/d ratio. The enhancement was more pronounced in CFRP-reinforced beams (approximately 15–20%) than in GFRP-reinforced beams (approximately 5–10%), highlighting the effect of higher stiffness reinforcement.

5. The energy absorption capacity of the beams was significantly affected by all investigated parameters. A decrease in the a/d ratio, an increase in concrete compressive

strength, and a higher reinforcement ratio all contributed to enhanced energy absorption. GFRP-reinforced beams showed greater sensitivity to parameter variations due to their higher deformability, whereas in CFRP-reinforced beams, energy absorption was more closely associated with increased load-carrying capacity.

6. Overall, the structural performance of deep beams is governed by the combined interaction of reinforcement type, geometric configuration, and material properties. While CFRP reinforcement provides superior strength and stiffness, GFRP reinforcement offers enhanced deformation capacity and energy dissipation. Therefore, the selection of reinforcement type should be based on the specific performance requirements of the structural system.

7. The selection of FRP reinforcement in reinforced concrete deep beams should be based on the targeted structural performance criteria. While CFRP reinforcement provides higher strength and stiffness, GFRP reinforcement offers greater ductility and energy absorption capacity. Accordingly, CFRP is more suitable for strength- and stiffness-dominated designs, whereas GFRP is advantageous in applications where deformation capacity and energy dissipation are critical. In addition, the use of hybrid reinforcement combining both types can be considered an effective design approach, as it has the potential to optimize structural performance by providing both high load-carrying capacity and improved deformation capacity.

Author Contributions: Conceptualization, M.Ö.; methodology, M.Ö. and Y.S.; validation, Y.S.; formal analysis, Y.S.; investigation, M.Ö. and Y.S.; resources, M.Ö.; data curation, Y.S.; writing—original draft preparation, Y.S.; writing—review and editing, M.Ö.; visualization, Y.S.; supervision, M.Ö.; project administration, M.Ö. All authors have read and agreed to the published version of the manuscript.

Funding: This research received no external funding.

Data Availability Statement: The data presented in this study are available on request from the corresponding author due to technical/time limitations.

Conflicts of Interest: The authors declare no conflicts of interest.

References

1. ACI Committee 318. *Building Code Requirements for Structural Concrete (ACI 318R-19)*; American Concrete Institute: Farmington Hills, MI, USA, 2022.
2. Rahim, N.I.; Mohammed, B.S.; Al-Fakih, A.; Wahab, M.M.A.; Liew, M.S.; Anwar, A.; Amran, Y.H.M. Strengthening the Structural Behavior of Web Openings in RC Deep Beam Using CFRP. *Materials* **2020**, *13*, 2804. [CrossRef]
3. Al-Mahbashi, M.; Abbas, H.; Elsanadedy, H.; Abadel, A.; Alrubaidi, M.; Almusallam, T.; Al-Salloum, Y. Structural Response of Continuous High-Strength Concrete Deep Beams with Rectangular Web Openings. *Buildings* **2026**, *16*, 38. [CrossRef]
4. Sammen, S.S.; Ahmed, O.W.; Al-Karawi, S.N. Nonlinear Finite Element Analysis of Concrete Beam Reinforced with Fiber Reinforced Polymer (FRM). *IOP Conf. Ser. Mater. Sci. Eng.* **2019**, *518*, 022086. [CrossRef]
5. Elbawab, Y.; Elbawab, Y.; El Zoughby, Z.; ElKadi, O.; AbouZeid, M.; Sayed-Ahmed, E. Flexural Testing of Steel-, GFRP-, BFRP-, and Hybrid Reinforced Beams. *Polymers* **2025**, *17*, 2027. [CrossRef]
6. John, S.K.; Cascardi, A.; Verre, S.; Nadir, Y. RC Columns Subjected to Lateral Cyclic Force with Different FRCM-Strengthening Schemes: Experimental and Numerical Investigation. *Bull. Earthq. Eng.* **2025**, *23*, 1561–1590. [CrossRef]
7. Nerilli, F.; Ahmadi, H.M.; Imperatore, S.; Vairo, G. Bond–Slip Performance of GFRP Rebars in Concrete Under Alkaline and Thermal Conditioning. *J. Compos. Sci.* **2026**, *10*, 131. [CrossRef]
8. Sümer, Y.; Öztemel, M. Investigation of the Effect of GFRP Reinforcement Bars on the Flexural Strength of Reinforced Concrete Beams Using the Finite Element Method. *Fibers* **2025**, *13*, 125. [CrossRef]
9. Abed, F.; El-Chabib, H.; AlHamaydeh, M. Shear characteristics of GFRP-reinforced concrete deep beams without web reinforcement. *J. Reinf. Plast. Compos.* **2012**, *31*, 1063–1073. [CrossRef]
10. Abbas, A.L.; Ahmed, Q.W.; Salman, W.D. Nonlinear Behavior of Reinforced Concrete Deep Beams Reinforced with Internal Fiber-Reinforced Polymer. *Int. J. Civ. Eng. Technol.* **2018**, *9*, 2811–2825.

11. Sheikh-Sobeh, A.; Kachouh, N.; El-Maaddawy, T. Numerical Analysis of Concrete Deep Beams Reinforced with Glass Fiber-Reinforced Polymer Bars. *Buildings* **2023**, *13*, 2767. [CrossRef]
12. Hanoon, A.N.; Jaafar, M.S.; Hejazi, F.; Abd Aziz, F.N.A. Strut Effectiveness Factor for Reinforced Concrete Deep Beams under Dynamic Loading Conditions. *Case Stud. Struct. Eng.* **2016**, *6*, 84–102. [CrossRef]
13. Kazemi, M.; Daneshfar, M.; Zandi, Y.; Sadighi Agdas, A.; Yousefieh, N.; Mohammadifar, L.; Rahmani, A.; Saberian, M.; Mamdouh, A.; Khadimallah, M.A.; et al. Effects of the Concrete Strength and FRP Reinforcement Type on the Non-Linear Behavior of Concrete Deep Beams. *Sustainability* **2022**, *14*, 4136. [CrossRef]
14. Sogut, K. Structural Behaviour of Concrete Deep Beams Reinforced with Aluminium Alloy Bars. *Appl. Sci.* **2025**, *15*, 5453. [CrossRef]
15. Mirzaaghabeik, H.; Mashaan, N.S.; Shukla, S.K. Shear Behavior of Ultra-High-Performance Concrete Deep Beams Reinforced with Fibers: A State-of-the-Art Review. *Infrastructures* **2025**, *10*, 67. [CrossRef]
16. Saingam, P.; Ejaz, A.; Gadagamma, C.K.; Hussain, Q.; Sua-iam, G.; Chatveera, B.; Maneengamlert, B.; Joyklad, P. Innovative Approaches to RC Deep Beam Strengthening: Evaluating Low-Cost Glass Fiber Wraps Against Traditional CFRP Solutions. *Polymers* **2025**, *17*, 807. [CrossRef]
17. Hamoda, A.; Yehia, S.A.; Ahmed, M.; Sennah, K.; Abadel, A.A.; Shahin, R.I. Experimental and Numerical Investigation of Shear Strengthening of Simply Supported Deep Beams Incorporating Stainless Steel Plates. *Buildings* **2024**, *14*, 3680. [CrossRef]
18. Tawfik, A.B.; Mahfouz, S.Y.; Taher, S.E.-D.F. Nonlinear ABAQUS Simulations for Notched Concrete Beams. *Materials* **2021**, *14*, 7349. [CrossRef]
19. Yu, T.; Teng, J.G.; Wong, Y.L.; Dong, S.L. Finite Element Modeling of Confined Concrete—II: Plastic-Damage Model. *Eng. Struct.* **2010**, *32*, 680–691. [CrossRef]
20. Lee, J.; Fenves, G.L. Plastic-Damage Model for Cyclic Loading of Concrete Structures. *J. Eng. Mech.* **1998**, *124*, 892–900. [CrossRef]
21. Lubliner, J.; Oliver, J.; Oller, S.; Oñate, E. A plasticdamage model for concrete. *Int. J. Solids Struct.* **1989**, *25*, 299–326. [CrossRef]
22. Hibbitt, H.; Karlsson, B.; Sorensen, E. *ABAQUS User's Manual*; Dassault Systèmes Simulia Corp.: Providence, RI, USA, 2012.
23. Abaqus/CAE. *Abaqus Analysis User's Guide*; Dassault Systèmes Simulia Corp.: Providence, RI, USA, 2022.
24. Aktaş, M.; Sümer, Y. Nonlinear Finite Element Analysis of Damaged and Strengthened Reinforced Concrete Beams. *J. Civ. Eng. Manag.* **2014**, *20*, 201–210. [CrossRef]
25. Sümer, Y.; Aktaş, M. Defining Parameters for Concrete Damage Plasticity Model. *Chall. J. Struct. Mech.* **2015**, *1*, 149–155. [CrossRef]
26. Mander, J.B.; Priestley, M.J.N.; Park, R. Theoretical stress–strain model for confined concrete. *J. Struct. Eng.* **1988**, *114*, 1804–1826. [CrossRef]
27. Comite Euro-International du Beton (CEB). *CEB-FIP Model Code 1990 (CEB-FIP MC90)*; Bulletin d'Information No. 215; CEB: Lausanne, Switzerland, 1993.
28. Rots, J.G. Computational Modeling of Concrete Fracture. Ph.D. Thesis, Delft University of Technology, Delft, The Netherlands, 1988.
29. Andermatt, M.F.; Lubell, A.S. Behavior of Concrete Deep Beams Reinforced with Internal Fiber-Reinforced Polymer—Experimental Study. *ACI Struct. J.* **2013**, *110*, 585–594. [CrossRef]
30. Almusallam, T.H.; Elsanadedy, H.M.; Al-Salloum, Y.A.; Alsayed, S.H. Experimental and Numerical Investigation for the Flexural Strengthening of RC Beams Using Near-Surface Mounted Steel or GFRP Bars. *Constr. Build. Mater.* **2013**, *40*, 145–161. [CrossRef]
31. Kazemi, M.; Li, J.; Lahouti Haredasht, S.; Yousefieh, N.; Jahandari, S.; Saberian, M. Non-Linear Behaviour of Concrete Beams Reinforced with GFRP and CFRP Bars Grouted in Sleeves. *Structures* **2020**, *23*, 87–102. [CrossRef]
32. Clark, A.P. Diagonal tension in reinforced concrete beams. *ACI J.* **1951**, *48*, 145–156.

Disclaimer/Publisher's Note: The statements, opinions and data contained in all publications are solely those of the individual author(s) and contributor(s) and not of MDPI and/or the editor(s). MDPI and/or the editor(s) disclaim responsibility for any injury to people or property resulting from any ideas, methods, instructions or products referred to in the content.